

MODEL-BASED ITERATIVE RECONSTRUCTION AND DIRECT DEEP
LEARNING FOR ONE-SIDED ULTRASONIC NON-DESTRUCTIVE
EVALUATION

A Dissertation

Submitted to the Faculty

of

Purdue University

by

Hani A. Almansouri

In Partial Fulfillment of the

Requirements for the Degree

of

Doctor of Philosophy

December 2018

Purdue University

West Lafayette, Indiana

**THE PURDUE UNIVERSITY GRADUATE SCHOOL
STATEMENT OF DISSERTATION APPROVAL**

Dr. Charles Bouman, Chair

School of Electrical and Computer Engineering

Dr. Mark Bell

School of Electrical and Computer Engineering

Dr. James Krogmeier

School of Electrical and Computer Engineering

Dr. Michael Zoltowski

School of Electrical and Computer Engineering

Approved by:

Dr. Pedro Irazoqui

Head of the School Graduate Program

To my beloved parents.

ACKNOWLEDGMENTS

My sincere thanks to my major advisor, Prof. Charles Bouman, for all his support and guidance. I learned a lot from his vast knowledge and experience. I am very inspired by how he always look at the problem from a different angle. I really appreciate how patient he was with me in improving my arguments over and over in research. It has been a privilege to work with him.

I would also like to express my gratitude to the rest of my committee members: Prof. Mark Bell, Prof. James Krogmeier, and Prof. Michael Zoltowski. They have given me very helpful comments and guidance and taught me many courses that I needed in this research. I am really honored to have them in the committee.

My sincere thanks to Dr. Hector Santos-Villalobos and Dr. Singanallur Venkatakrishnan from Oak Ridge National Lab for giving me so much of their time. They have shared with me a lot from their invaluable experience in research. They have been great mentors and great friends.

Many thanks to my family and friends for all their support and encouragement. They have always been there for me. Many thanks to my niece and nephew, Lomair and Sinan, who I love so much, for all their best wishes and for being very interested in my work and my research.

I am profoundly grateful to my parents. They have always encouraged me and pushed me to be the best even though it meant studying abroad and being away from them for so many years. I owe all my accomplishments and success to them.

Heartfelt thanks to my wife and my best friend, Wejdan Alamri, for being with me in every step through this journey. Non of this would have happened without her support. She made this journey colorful with many wonderful memories.

My last words go to my baby boy, Omar. His smiles and laughs gave me all the energy I needed and kept me working tirelessly in my research. I am so grateful he is in my life.

TABLE OF CONTENTS

	Page
LIST OF TABLES	viii
LIST OF FIGURES	ix
ABBREVIATIONS	xiv
ABSTRACT	xv
1 MODEL-BASED ITERATIVE RECONSTRUCTION FOR ONE-SIDED ULTRASONIC NON-DESTRUCTIVE EVALUATION	1
1.1 Introduction	1
1.2 Forward Model of One-Sided UNDE	4
1.2.1 Direct Arrival Signal Artifacts	8
1.2.2 Anisotropic Propagation	9
1.2.3 Joint-MAP Stitching	12
1.3 Prior Model Of The Image	15
1.3.1 Non-linear Spatially-Variant Regularization	16
1.3.2 Selection of Prior Model Parameters	17
1.4 Optimization of MAP Cost Function	19
1.5 Results	20
1.5.1 Algorithms for Comparison	22
1.5.2 K-wave Simulated Results	23
1.5.3 MIRA Experimental Results	28
1.5.4 Results from Modifying the Forward and Prior Models	38
1.5.5 Convergence of MBIR	39
1.6 Summary	39
2 DIRECT DEEP LEARNING FOR ONE-SIDED ULTRASONIC NON-DESTRUCTIVE EVALUATION	42

	Page
2.1 Introduction	42
2.2 Ultrasound Forward Model and Linear Model-Based Inversion	45
2.3 Direct Deep Learning for Non-Linear Ultrasound Inversion	49
2.4 Modeling Mismatch	51
2.5 Spatially Variant Amplification for Input In DDL	53
2.6 Joint DDL	53
2.7 Results	55
2.7.1 Algorithms for Comparison	57
2.7.2 K-wave Simulated Results	60
2.7.3 MIRA Experimental Results	62
2.7.4 Results from Spatially Variant Amplification	68
2.8 Summary	73
REFERENCES	74
VITA	79

LIST OF TABLES

Table	Page	
1.1	Parameter settings for k-wave simulation.	27
1.2	Parameter settings used for all techniques to reconstruct the experimental MIRA data.	31
1.3	The l_1 -norm, 2D MBIR, and 2.5D MBIR parameter settings used in the simulated K-wave and the experimental MIRA data.	34
1.4	Precision vs recall area for all techniques in Fig. 1.11 and Fig. 1.18. MBIR has the highest PR area.	34
2.1	Parameter settings used for all techniques for the k-wave and the MIRA data.	69
2.2	The MBIR parameters settings used for the k-wave and the MIRA data.	69
2.3	Precision vs recall area for all techniques in Fig. 2.14 and Fig. 2.20. DDL has the highest PR area.	72

LIST OF FIGURES

Figure	Page
1.1 An illustration of a typical one-sided UNDE problem where $s(t)$ is the transmitted signal, ν is a point in the field-of-view, $y_{i,j}(\nu, t)$ is the received signal reflected from ν , θ_t is the angle between r_i and ν , and θ_r is the angle between r_j and ν	4
1.2 Example of a SAFT reconstruction from real data of a concrete structure. (a) shows the defect diagram containing steel rebars (dotted circles), defects (marked D#), and the back wall (dotted line). (b) shows SAFT reconstruction for a single scan of the large field-of-view in (a). (c) shows the SAFT reconstruction for the entire field-of-view after stitching the results from each individual scan.	5
1.3 A plot of the measured transmitter-receiver profile obtained from reflections from a point scatter from experimental data. The variable $T(v)$ is defined as $T(\nu) = \sqrt{\theta(\nu)_t^2 + \theta(\nu)_r^2}$ to project the 3D plot to a 2D plot for a better visualization.	10
1.4 Beam pattern model for an ultrasound transducer placed at (0,0) for isotropic propagation (left) and anisotropic propagation (right). Left image shows equal propagation in all direction. Right image shows more attenuation as the angle between the transmitter and the pixel increases.	11
1.5 A plot showing both the measured transmitter-receiver profile and the anisotropic model. The variable $T(v)$ is defined as $T(\nu) = \sqrt{\theta(\nu)_t^2 + \theta(\nu)_r^2}$ to project the 3D plot to a 2D plot.	11
1.6 An illustration of multiple measurements needed to scan a large field-of-view. Images from each scan share some pixels with its neighbor images. Proper stitching technique is needed to account for this shared areas in the field-of-view.	14
1.7 Back-projection of two point scatters, one that is closer to the transducers (17cm deep) and one that is far from the transducers (105 cm deep). As the reflection gets deeper, the lateral resolution decreases.	18
1.8 ICD algorithm using the majorization technique with shift error estimation (top red box) and direct arrival modeling (bottom red box) [30,31].	21

Figure	Page
1.9 Comparison between MBIR and SAFT reconstruction from the k-wave simulated data. The far left column is the position of the defects. The next column is SAFT reconstruction. The next column is l_1 -norm reconstruction. The far right column is MBIR reconstruction. MBIR tends to produce results with less noise and artifacts compared to SAFT and l_1 -norm.	25
1.10 Comparison between SAFT, l_1 -norm, MBIR reconstructions from the k-wave simulated data with different SNR. The defect diagram is the same as the defect diagram in Test 1 in Fig. 1.9. The left column is SAFT reconstruction. The next column is l_1 -norm reconstruction. The right column is MBIR reconstruction. Each row correspond to different SNR value where the SNR values from top to bottom are 3, 1, and 0.33, respectively. MBIR tends to produce results with less noise and artifacts compared to SAFT and l_1 -norm.	26
1.11 PR curves for each technique over all 4 tests in Fig.1.9. MBIR outperforms the other techniques by having the highest PR area.	27
1.12 The concrete specimen and the MIRA device used for the experimental data [33]. 20 defects are embedded in the specimen.	31
1.13 Type and legend for each defect [33]. These defects are embedded in the concrete specimen.	32
1.14 Smooth side view of defects [33]. The location of the defects is approximated due to possible displacement while pouring the cement.	33
1.15 Depth view of defects, smooth side on the right and rough side on the left, [33]. The location of the defects is approximated due to possible displacement while pouring the cement.	33
1.16 A picture of defect 12 before embedding it in the specimen, [33]. It is made of dissolving styrofoam.	34
1.17 Comparison between all reconstruction results from the MIRA experimental data: the first row from the top is the position of the defects, the second row is SAFT reconstruction, the third row is l_1 -norm reconstruction, the fourth row is 2D MBIR reconstruction, and the fifth row is 2.5D MBIR reconstruction. 2.5D and 2D MBIR tend to produce results with less noise and artifacts compared to other techniques.	35
1.18 PR curves for each technique over all 73 slices in the MIRA experimental data. 2.5D and 2D MBIR outperforms the other techniques.	36

Figure	Page
1.19 A comparison between different settings of MBIR where (a) is the defect diagram of rough-hor-slice11, (b) is 2D MBIR reconstruction, (c) is 2.5D MBIR reconstruction with all modifications to the forward and prior models, (d) is 2D MBIR reconstruction without direct arrival signal or shift error estimation, (e) is 2D MBIR reconstruction without shift error estimation, (f) is 2D MBIR reconstruction using regular stitching, (g) is 2D MBIR reconstruction using an isotropic model, (h) is 2D MBIR reconstruction for a constant regularization. The results in (c) shows performance enhancement over the other results.	37
1.20 NRMSE vs. iteration for different initializations in the MBIR algorithm. The initializations used in the plot are uniformly distributed random noise with range $[0, 10]$, zero, and a constant value of 10, respectively.	40
2.1 Illustration of a widely used ultrasound system for one-sided non-destructive evaluation using a multi-static array. The transducers are used to make pulse-echo measurements which are processed to reconstruct the cross-section.	44
2.2 Illustration of raw data (arranged to form a 2D image) obtained from PWI and multi-static array using 10 transducers. (a) is the ground truth image. (b) is the raw data obtained from PWI where each column correspond to the received signal at one transducer. (c) is the raw data obtained from multi-static array where each column corresponds to one transmit-receive pair.	45
2.3 Illustration of a back-projection of a one-sided ultrasonic NDE measurements using the system matrix A in Eq. 2.3. The left image is the ground truth (speed-of-sound in units of m/s) and the right image is the back-projection of the simulated measurements obtained from the ground truth using an array of 10 transducers and a non-linear wave propagation model. The back-projection suffers from artifacts and does not faithfully reconstruct the object.	47
2.4 DDL architecture used for the reconstructions. The input is an image obtained by applying the adjoint of a linear operator to the measurements. Within each stage, we apply a 3×3 convolution followed by a batch normalization and a rectified linear unit. The size of the feature maps at each stage is noted in the image.	48
2.5 Illustration of k-wave simulated data.	50
2.6 Illustration of DDL training from k-wave PSI training data.	50
2.7 Illustration of k-wave modeling mismatch with real data. The k-wave plot is from a k-wave simulation from a generated ground truth similar to a ground truth in the MIRA real data in [39].	52

Figure	Page
2.8 Illustration of noisy-simulation-input (NSI) k-wave where AWGN is added to the input of k-wave before simulation. This block should replace the PSI k-wave block in Fig. 2.6 to generate NSI data.	52
2.9 An illustration of multiple measurements needed to scan a cross-section. Images from each scan share some pixels with its neighbor images. Proper stitching technique is needed to account for this shared areas in the field-of-view.	55
2.10 Illustration of Joint-DDL architecture. Within each stage, we apply a 3×3 convolution followed by a batch normalization and a rectified linear unit. The size of the feature maps at each stage is noted in the image. The input to the neural network contains multiple channels where each channel is a back-projection of one of the scans shifted in the correct region where the scan was performed.	56
2.11 An illustration of generating dataset of dependent cross-sections (CS). This helps in reducing the number of scans and simulations needed for DDL training.	56
2.12 Example of training phantoms used to train DDL and a plot of the training and validation loss vs. epoch.	60
2.13 Comparison between all reconstruction results from k-wave simulated data from the test set only: the first row is the ground truth, the second row is SAFT reconstruction, the third row is linear MBIR reconstruction, the fourth row is PSI-DDL reconstruction, and the fifth row is NSI-DDL reconstruction. PSI-DDL is outperforming the other techniques in showing target shapes much closer to the ground truth shapes.	63
2.14 PR plots for results from the entire k-wave PSI testing data.	64
2.15 Comparison between all techniques on reconstructing sample 1 in Fig. 2.13 with AWGN added to the measurements of sample 1 with different SNR values: the first row is SAFT reconstruction, the second row is linear MBIR reconstruction, the third row is PSI-DDL reconstruction, and the fourth row is NSI-DDL reconstruction.	65
2.16 Comparison between all techniques on reconstructing sample 1 in Fig. 2.13 with different number of transmitter-receiver pairs (less than 45 distinct pairs) per scan: the first row is SAFT reconstruction, the second row is linear MBIR reconstruction, the third row is PSI-DDL reconstruction, and the fourth row is NSI-DDL reconstruction.	66
2.17 The concrete specimen and the MIRA device used for the experimental data [33]. 20 defects are embedded in the specimen.	70

Figure	Page
2.18 A side view of defects [33]. The location of the defects is approximated due to possible displacement while pouring the cement.	70
2.19 Comparison between all techniques in reconstructing real data: the first row is the ground truth, the second row is SAFT reconstruction, the third row is linear MBIR reconstruction, the fourth row is PSI-DDL reconstruction, and the fifth row is NSI-DDL reconstruction. MBIR appears to have less noise while NSI-DDL appears to show more targets and less artifacts. The reconstructed targets in NSI-DDL have closer shapes to the real targets.	71
2.20 PR plots for the entire MIRA experimental results.	72
2.21 Results for sample 1 in Fig. 2.19 for DDL with and without SVA. (a) is NSI-DDL without SVA and (b) is NSI-DDL with SVA.	72

ABBREVIATIONS

NDE	non-destructive evaluation
UNDE	ultrasonic non-destructive evaluation
SAFT	synthetic aperture focusing technique
DAS	delay and sum
MBIR	model based iterative reconstruction
QGGMRF	q-generalized Gaussian Markov random field
ICD	iterative coordinate descent
PR	precision and recall
SNR	signal to noise ratio
NRMSE	normalized root mean square error
CNN	convolutional neural network
DDL	direct deep learning

ABSTRACT

Almansouri, Hani A. PhD, Purdue University, December 2018. Model-Based Iterative Reconstruction and Direct Deep Learning for One-Sided Ultrasonic Non-Destructive Evaluation. Major Professor: Charles A. Bouman.

One-sided ultrasonic non-destructive evaluation (UNDE) is extensively used to characterize structures that need to be inspected and maintained from defects and flaws that could affect the performance of power plants, such as nuclear power plants. Most UNDE systems send acoustic pulses into the structure of interest, measure the received waveform and use an algorithm to reconstruct the quantity of interest. The most widely used algorithm in UNDE systems is the synthetic aperture focusing technique (SAFT) because it produces acceptable results in real time. A few regularized inversion techniques with linear models have been proposed which can improve on SAFT, but they tend to make simplifying assumptions that show artifacts and do not address how to obtain reconstructions from large real data sets. In this thesis, we present two studies. The first study covers the model-based iterative reconstruction (MBIR) technique which is used to resolve some of the issues in SAFT and the current linear regularized inversion techniques, and the second study covers the direct deep learning (DDL) technique which is used to further resolve issues related to non-linear interactions between the ultrasound signal and the specimen.

In the first study, we propose a model-based iterative reconstruction (MBIR) algorithm designed for scanning UNDE systems. MBIR reconstructs the image by optimizing a cost function that contains two terms: the forward model that models the measurements and the prior model that models the object. To further reduce some of the artifacts in the results, we enhance the forward model of MBIR to account for the direct arrival artifacts and the isotropic artifacts. The direct arrival signals

are the signals received directly from the transmitter without being reflected. These signals contain no useful information about the specimen and produce high amplitude artifacts in regions close to the transducers. We resolve this issue by modeling these direct arrival signals in the forward model to reduce their artifacts while maintaining information from reflections of other objects. Next, the isotropic artifacts appear when the transmitted signal is assumed to propagate in all directions equally. Therefore, we modify our forward model to resolve this issue by modeling the anisotropic propagation. Next, because of the significant attenuation of the transmitted signal as it propagates through deeper regions, the reconstruction of deeper regions tends to be much dimmer than closer regions. Therefore, we combine the forward model with a spatially variant prior model to account for the attenuation by reducing the regularization as the pixel gets deeper. Next, for scanning large structures, multiple scans are required to cover the whole field of view. Typically, these scans are performed in raster order which makes adjacent scans share some useful correlations. Reconstructing each scan individually and performing a conventional stitching method is not an efficient way because this could produce stitching artifacts and ignore extra information from adjacent scans. We present an algorithm to jointly reconstruct measurements from large data sets that reduces the stitching artifacts and exploits useful information from adjacent scans. Next, using simulated and extensive experimental data, we show MBIR results and demonstrate how we can improve over SAFT as well as existing regularized inversion techniques. However, even with this improvement, MBIR still results in some artifacts caused by the inherent non-linearity of the interaction between the ultrasound signal and the specimen.

In the second study, we propose DDL, a non-iterative model-based reconstruction method for inverting measurements that are based on non-linear forward models for ultrasound imaging. Our approach involves obtaining an approximate estimate of the reconstruction using a simple linear back-projection and training a deep neural network to refine this to the actual reconstruction. While the technique we are proposing can show significant enhancement compared to the current techniques with

simulated data, one issue appears with the performance of this technique when applied to experimental data. The issue is a modeling mismatch between the simulated training data and the real data. We propose an effective solution that can reduce the effect of this modeling mismatch by adding noise to the simulation input of the training set before simulation. This solution trains the neural network on the general features of the system rather than specific features of the simulator and can act as a regularization to the neural network. Another issue appears similar to the issue in MBIR caused by the attenuation of deeper reflections. Therefore, we propose a spatially variant amplification technique applied to the back-projection to amplify deeper regions. Next, to reconstruct from a large field of view that requires multiple scans, we propose a joint deep neural network technique to jointly reconstruct an image from these multiple scans. Finally, we apply DDL to simulated and experimental ultrasound data to demonstrate significant improvements in image quality compared to the delay-and-sum approach and the linear model-based reconstruction approach.

1. MODEL-BASED ITERATIVE RECONSTRUCTION FOR ONE-SIDED ULTRASONIC NON-DESTRUCTIVE EVALUATION

1.1 Introduction

One-sided ultrasonic non-destructive evaluation (UNDE) is widely used in many applications to characterize and detect flaws in materials, such as concrete structures in nuclear power plants (NPP), because of its low cost, high penetration, portability, and safety compared with other NDE methods [1–3]. A typical one-sided UNDE system consists of a sensor that transmits sound waves into the structures of interest and an array of receivers that measures the reflected signals (see Fig. 1.1). Such a set up is scanned across a large surface in a rectangular grid pattern and the reflected signals from each position are processed to reconstruct the underlying structure. The ability to easily probe structures that can only be accessed from a single side combined along with the ability of ultrasound signals to penetrate deep into structures make one-sided UNDE a powerful tool for the analysis of structures across a variety of applications [4, 5].

Reconstruction of structures from one-sided UNDE systems are challenging because of the complex interaction of ultrasound waves with matter, the geometry of the experimental set-up, the trade-off between resolution and penetration, and the potentially low signal-to-noise ratio of the received signals [6, 7]. The most widely used reconstruction method for UNDE is the synthetic aperture focusing technique (SAFT) [4, 8–12]. SAFT uses a delay-and-sum (DAS) approach to reconstruct ultrasound images. Fig. 1.2 shows an example of a SAFT reconstruction from real data. Notice that SAFT reconstructions tend to have significant artifacts due to the fact that SAFT assumes a simple propagation model and does not account for

a variety of effects such as noise and image statistics, direct arrival signal artifacts, reverberation, and shadowing [11, 12]. In summary, while SAFT is computationally inexpensive to implement, it can result in significant artifacts in the one-sided UNDE reconstructions.

In order to overcome some of the short-comings of the SAFT method, regularized iterative reconstruction methods that use linear models (due to their low computational complexity) have recently been proposed for various ultrasound inverse problems. These methods formulate the reconstruction as minimizing a cost-function that balances a data fidelity term with a regularization applied to the image/volume to be reconstructed. The data fidelity term encodes a physics based model to reduce the error between the measurements and the projected reconstruction while the regularizer forces certain constraints on the reconstruction itself. For the data fidelity term, regularized iterative techniques for one-sided UNDE, such as [13, 14], use a simple linear model that models the propagation of the ultrasonic wave to reconstruct the reflectance B-mode images. A technique that uses the same forward model, but shows 2D images for a fixed depth (c-mode), is shown in [15]. The forward model in [15] has been upgraded to account for the beam profile as in [16] which can help in reducing some artifacts. However, this forward model does not account for direct arrival signals caused by coupling the ultrasonic device to the surface of the structure which can cause artifacts and interference with reflections. Furthermore, the reconstruction algorithm of [16] is not designed to exploit correlations between adjacent scans for systems with large field-of-view.

In [14, 16–18], the authors used a simple regularization terms, such as l_1 or l_2 . This regularization is suitable for imaging point scatters or sparse regions. However, for more complex medium where edge preservation is needed, other techniques use a more sophisticated regularization, such as total variation, where they showed significant enhancement over SAFT [13, 15]. The method in [13] uses total variation with variety of a regularization terms that are depth dependent to resolve the attenuation and blurring for deeper reflections. However, the depth-dependent regularization is

linear with depth which might not be the best modeling for the depth attenuation. Therefore, while regularized inversion methods that use a linear forward model have shown promise in certain applications, they do not deal with the direct arrival signal artifacts in a principled manner, they have not been designed to jointly handle large data sets that require multiple scanning for one-sided UNDE systems, and they do not fully account for the depth-dependent blurring that can occur by the use of certain regularizers.

In this thesis, we propose an ultrasonic model-based iterative reconstruction (MBIR) algorithm designed specifically for one-sided UNDE systems of large structures. We resolve the issues discussed above by enhancing the forward and prior models used in the current regularized iterative techniques. The enhancements to the forward model include a direct arrival signal model with varying acoustic speed and an anisotropic model of the transmitted signal propagation to reduce artifacts in the reconstruction. Also, we repopulate the system matrix of the forward model to generate a larger system matrix for larger field of views to share more information about adjacent scans which can help in reducing noise and artifacts and enhancing the reconstruction. Furthermore, the prior model is enhanced by increasing and conveniently controlling the regularization for deeper regions to reduce the attenuation to these regions. In previous work, we have demonstrated the performance of MBIR compared with SAFT using different combinations of these enhancements [19–21]. We introduce four major contributions in this thesis:

- 1) A physics-based linear forward model that models the direct arrival signal with varying acoustic speed, absorption attenuation, and anisotropic propagation;
- 2) A non-linear spatially-variant regularization to enhance the reconstruction for deeper regions;
- 3) A systematic way to reconstruct the volume from all the measured data simultaneously rather than individual reconstruction using joint-MAP stitching and 2.5D MBIR;

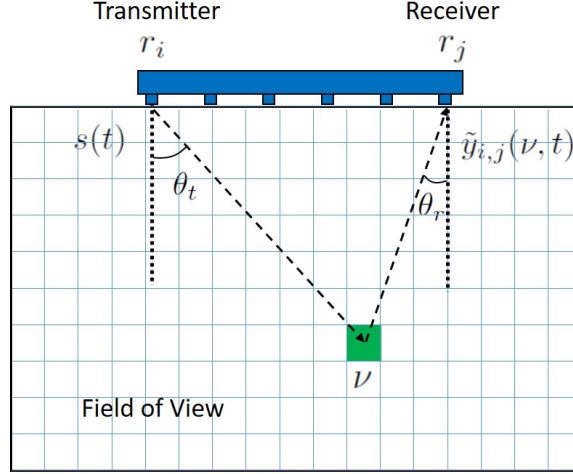


Fig. 1.1. An illustration of a typical one-sided UNDE problem where $s(t)$ is the transmitted signal, ν is a point in the field-of-view, $y_{i,j}(\nu, t)$ is the received signal reflected from ν , θ_t is the angle between r_i and ν , and θ_r is the angle between r_j and ν .

4) Qualitative and quantitative results from simulated and extensive experimental data.

The thesis is organized as follows. In section 1.2 we cover the design for the forward model of the ultrasonic MBIR for one-sided NDE applications. In section 1.3 we cover the prior model used for MBIR. In section 1.4 we cover the optimization of the MAP cost function using the ICD method. In section 1.5 we cover simulated and experimental results from MBIR and other techniques. In section 1.6 we cover the conclusion.

1.2 Forward Model of One-Sided UNDE

The reconstruction in an MBIR setting is given by the following minimization problem,

$$x_{MAP} = \arg \min_{(x)} \{-\log p(y|x) - \log p(x)\},$$

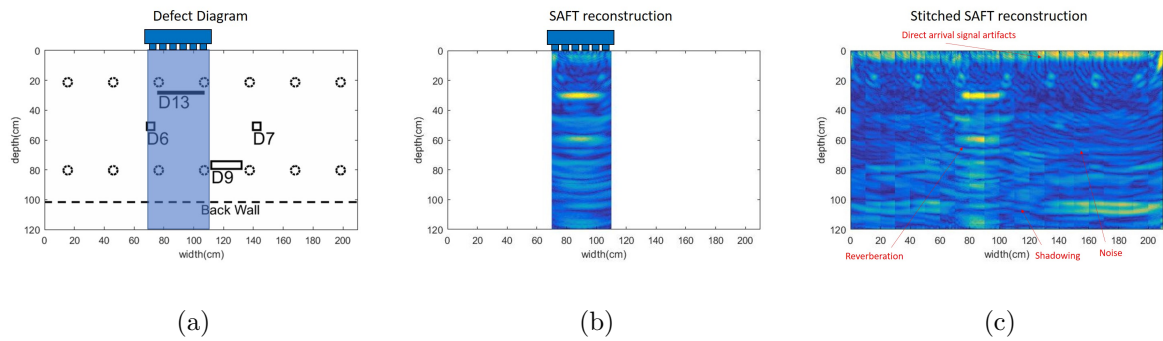


Fig. 1.2. Example of a SAFT reconstruction from real data of a concrete structure. (a) shows the defect diagram containing steel re-bars (dotted circles), defects (marked D#), and the back wall (dotted line). (b) shows SAFT reconstruction for a single scan of the large field-of-view in (a). (c) shows the SAFT reconstruction for the entire field-of-view after stitching the results from each individual scan.

where x is the image to be reconstructed, y is the measured data, x_{MAP} is the reconstructed image, $p(y|x)$ is the forward model and the probability distribution of y given x , $p(x)$ is the prior model and the probability distribution of x . The forward model is designed in the following way. We will consider a one-sided UNDE for a concrete structure where the transducers are coupled to the surface as shown in Fig. 1.1. We will consider a pressure signal (Pascal) transmitted from transducer i located at position $r_i \in \mathbb{R}^3$, reflected by a point located at $\nu \in \mathbb{R}^3$, and received by transducer j located at $r_j \in \mathbb{R}^3$. We assume the Fourier transform of the temporal impulse response of a system sending a signal from r_i and receiving from ν to be

$$G(r_i, \nu, f) = \lambda e^{-(\alpha(f)+j\beta(f))\|\nu-r_i\|}$$

where λ is a transmittance coefficient,

$$\alpha(f) = \alpha_0|f| \quad (\text{m}^{-1})$$

is the rate of attenuation,

$$\beta(f) = \frac{2\pi f}{c} \quad (\text{m}^{-1})$$

is the phase delay due to propagation through the specimen, and c is the speed of sound [22–28]. Similarly, we assume the Fourier transform of the impulse response of a system sending a signal from ν and receiving from r_j to be

$$G(\nu, r_j, f) = \lambda e^{-(\alpha(f)+j\beta(f))\|r_j-\nu\|} .$$

Assuming $s(t)$ (Pascal) is the input to the system and $\tilde{x}(\nu)$ (m^{-3}) is the reflectivity coefficient for ν , then the output $\tilde{Y}_{i,j}(\nu, f)$ ($\text{Pascal} \cdot \text{m}^{-3} \cdot \text{Hz}^{-1}$) at the receiver due to ν is

$$\begin{aligned} \tilde{Y}_{i,j}(\nu, f) &= -S(f)G(r_i, \nu, f)\tilde{x}(\nu)G(\nu, r_j, f) \\ &= -\lambda^2\tilde{x}(\nu)S(f)e^{-(\alpha_0c|f|+j2\pi f)\tau_{i,j}(\nu)}, \end{aligned}$$

where

$$\tau_{i,j}(\nu) = \frac{\|\nu - r_i\| + \|\nu - r_j\|}{c} \quad (\text{s}).$$

By defining

$$\tilde{h}(\tau_{i,j}(\nu), t) = \mathcal{F}^{-1} \left\{ -\lambda^2 S(f) e^{-\alpha_0 c |f| \tau_{i,j}(\nu)} \right\}, \quad (1.1)$$

where \mathcal{F}^{-1} is the inverse Fourier transform, the time domain output signal, $\tilde{y}_{i,j}(\nu, t)$ (Pascal \cdot m⁻³), is given by

$$\tilde{y}_{i,j}(\nu, t) = \tilde{h}(\tau_{i,j}(\nu), t - \tau_{i,j}(\nu)) \tilde{x}(\nu).$$

Note that $\tilde{h}(\tau_{i,j}(\nu), t)$ is a function of $\tau_{i,j}$ and t , i.e. not directly a function of ν . This is a very useful property that can reduce the computational cost of evaluating \tilde{h} . In many cases, $\tilde{h}(\tau, t)$ for any τ is close to zero after a certain time t_0 . In this case, it is very helpful to modify the previous equation to

$$\tilde{y}_{i,j}(\nu, t) = h(\tau_{i,j}(\nu), t - \tau_{i,j}(\nu)) \tilde{x}(\nu).$$

where

$$h(\tau, t) = \tilde{h}(\tau, t) \operatorname{rect} \left(\frac{t}{t_0} - \frac{1}{2} \right),$$

$$\operatorname{rect}(x) = 1 \text{ for } |x| < \frac{1}{2} \text{ and } 0 \text{ for } |x| \geq \frac{1}{2},$$

and t_0 is a constant where we assume $h(\tau, t)$ is equal to zero for $t > t_0$. Applying the rect function is very helpful in increasing the sparsity of the system matrix which leads to a dramatic decrease in memory and processing time. To get the overall output $\tilde{y}_{i,j}(t)$ (Pascal) from all points in \mathbb{R}^3 , we need to integrate over all ν :

$$\tilde{y}_{i,j}(t) = \int_{\mathbb{R}^3} \tilde{y}_{i,j}(\nu, t) d\nu \quad (1.2)$$

$$= \int_{\mathbb{R}^3} \tilde{A}_{i,j}(\tau_{i,j}(\nu), t) \tilde{x}(\nu) d\nu, \quad (1.3)$$

where

$$\tilde{A}_{i,j}(\tau_{i,j}(\nu), t) = h(\tau_{i,j}(\nu), t - \tau_{i,j}(\nu)). \quad (1.4)$$

For simplicity, the set of all transducer pairs, $\{i, j\}$, is mapped to the ordered set $\{1, \dots, K\}$, where K is the total number of transducer pairs. Hence, Eq. 1.3 becomes

$$\tilde{y}_k(t) = \int_{\mathbb{R}^3} \tilde{A}_k(\tau_k(\nu), t) \tilde{x}(\nu) d\nu. \quad (1.5)$$

Finally, we assume the noise associated with the measurements to be i.i.d. Gaussian.

1.2.1 Direct Arrival Signal Artifacts

When the ultrasonic device is attached or coupled to the surface of the concrete, a direct arrival signal is generated along with the transmitted signal. This direct arrival signal produces artifacts on the reconstructed image in regions closer to the transducer and it might interfere with some of the reflected signals (see Fig. 1.2). Eq. 1.5 models the output from the reflection of all points. However, the equation does not account for the direct arrival signal. Locating and deleting the direct arrival signal from the received signal eliminates the artifacts, but might lead to deleting reflection signals for closer objects. We propose a modification to the forward model that models the direct arrival signal and attenuates the artifact while preserving information from reflected signals. The modification adds the following term to the forward model in Eq. 1.5 that corresponds to the direct arrival signal,

$$\tilde{y}_k(t) = \int_{\mathbb{R}^3} \tilde{A}_k(\tau_k(\nu), t) \tilde{x}(\nu) d\nu + \tilde{d}_k(t) g_k, \quad (1.6)$$

where $\tilde{d}_k(t)$ is an additional term used to model the direct arrival signal given by

$$\begin{aligned} \tilde{d}_k(t) &= -\tilde{A}_k(\tau_k, t), \\ \tau_k &= \frac{\|r_i - r_j\|}{c}, \end{aligned}$$

and g_k is an unknown scaling coefficient for the direct arrival signal.

The above model works efficiently when the acoustic speed is constant. For a non-homogeneous material, such as concrete, the acoustic speed is not constant. This change in acoustic speed changes the location of the direct arrival signal and causes a mismatch with MBIR's direct arrival signal modeling. We can estimate the shift

error by searching for the delay that produces the maximum autocorrelation of the direct arrival signal,

$$\hat{l} = \arg \max_{-\tilde{\tau} \leq l \leq \tilde{\tau}} \left\{ \int \tilde{y}_k(t) \tilde{d}_k(t-l) dt \right\}$$

$$\tilde{d}_k(t) \leftarrow \tilde{d}_k(t - \hat{l}),$$

where $\tilde{\tau}$ is chosen to be small, e.g. 3 sampling periods, to insure the shift is within the integral boundaries and to avoid interfering with later reflections. This estimate finds the shift error with the assumption that reflections do not interfere with the direct arrival signal. Therefore, for homogeneous medium, our approach is able to reduce direct arrival signal artifacts and detect reflections close to the transducers. However, for non-homogenous medium, our approach is able to reduce direct arrival signal artifacts that do not interfere with reflections.

1.2.2 Anisotropic Propagation

Many models used in UNDE assume that the profile of the transmitted beam is isotropic [15, 29]. However, this assumption is not valid for many systems and it can produce artifacts. While it would be ideal to know the precise profile especially of the transmitted beam, in one-sided systems that we deal with, this is not known. However, we were able to measure a transmitter-receiver profile obtained from the reflections of one point scatter from different angles. Fig. 1.3 shows the normalized transmitter-receiver profile projected from a 3D to a 2D plot for a better visualization. The transmitter-receiver profile was measured by measuring the angle between the transmitter and the point scatter, $\theta_t(\nu)$, the angle between the receiver and the point scatter, $\theta_r(\nu)$, and the amplitude of the reflection from the point scatter. Fig. 1.1 shows illustration of $\theta_t(\nu)$ and $\theta_r(\nu)$. To model this transmitter-receiver profile, we adopted a similar apodization function as in [4] for the anisotropic model. However, the apodization function used in [4] has a slow attenuating window. In our application, a faster attenuating window is needed. We use an anisotropic beam pattern model as shown in Fig. 1.4. We define a function, $\phi_k(\nu)$, that has a value ranging from

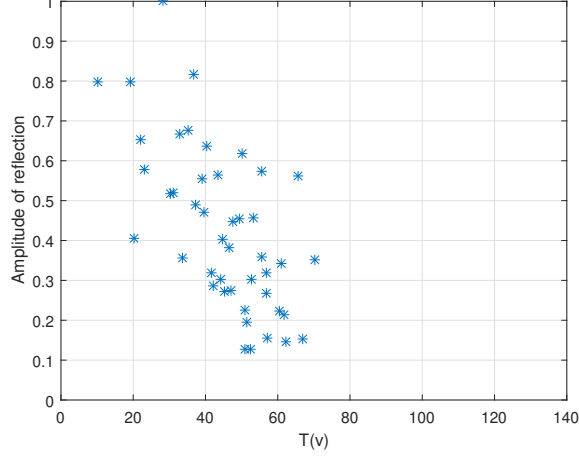


Fig. 1.3. A plot of the measured transmitter-receiver profile obtained from reflections from a point scatterer from experimental data. The variable $T(v)$ is defined as $T(v) = \sqrt{\theta(v)_t^2 + \theta(v)_r^2}$ to project the 3D plot to a 2D plot for a better visualization.

0 to 1. This function depends on the angles from the transmitter to ν and from ν to the receiver. $\phi_k(\nu)$ is monotonically decreasing with respect to those two angles. $\phi_k(\nu)$ can act as an attenuating window, such as cosine or Gaussian windows, to the output. The function $\phi_k(\nu)$ is added to Eq. 1.4 as follows:

$$\tilde{A}_k(\tau_k(\nu), t) = h(\tau_k(\nu), t - \tau_k(\nu))\phi_k(\nu). \quad (1.7)$$

Note that the beam pattern is assumed to be reciprocal, i.e. the receiver will also have the same beam pattern. In this thesis, we chose $\phi_k(\nu)$ to be

$$\phi_k(\nu) = a \cos^b(\theta_t(\nu)) \cos^b(\theta_r(\nu)) \quad ,$$

where a and b are constants. We performed a least square fit to calculate the value of a and b based on the measured transmitter-receiver profile. The calculated values were $a = 0.75$ and $b = 1.65$. Fig. 1.5 shows a plot of the measured transmitter-receiver profile and the anisotropic model with the least square fit of a and b . In this thesis, the value of a is set to 1 since it is a scalar applied to all pixels, and b is rounded up to the nearest integer, i.e $b = 2$.

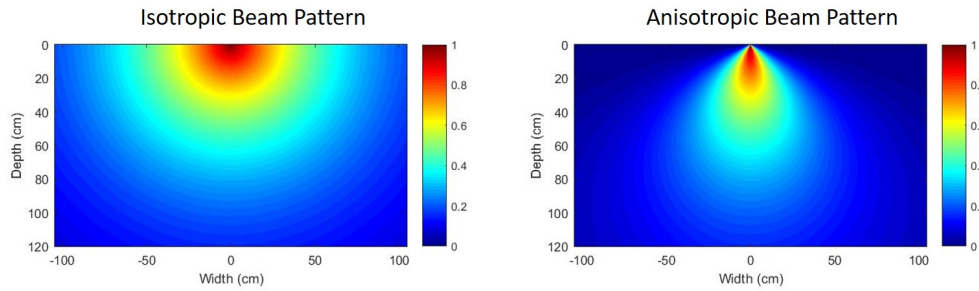


Fig. 1.4. Beam pattern model for an ultrasound transducer placed at (0,0) for isotropic propagation (left) and anisotropic propagation (right). Left image shows equal propagation in all direction. Right image shows more attenuation as the angle between the transmitter and the pixel increases.

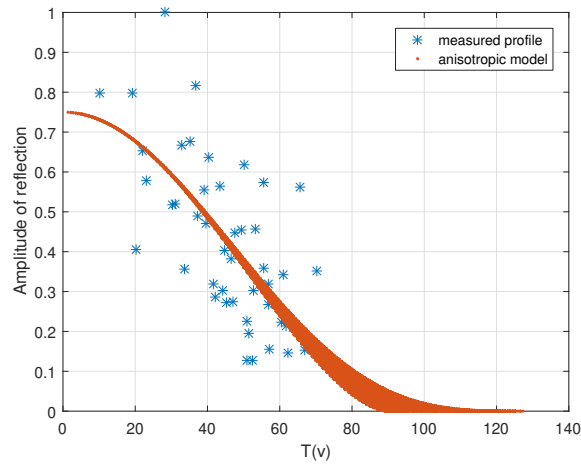


Fig. 1.5. A plot showing both the measured transmitter-receiver profile and the anisotropic model. The variable $T(\nu)$ is defined as $T(\nu) = \sqrt{\theta(\nu)_t^2 + \theta(\nu)_r^2}$ to project the 3D plot to a 2D plot.

Finally, the discretized version of the forward model can be used in the MAP estimate as shown below,

$$-\log p(y|x) = \frac{1}{2\sigma^2} \|y - Ax - Dg\|^2 + \text{constant},$$

where $y \in \mathbb{R}^{MK \times 1}$ is the measurement, σ^2 is the variance of the measurement, $A \in \mathbb{R}^{MK \times N}$ is the forward model (system matrix), $x \in \mathbb{R}^{N \times 1}$ is the image, $D \in \mathbb{R}^{MK \times K}$ is the direct arrival signal modeling matrix, $g \in \mathbb{R}^{K \times 1}$ is a vector containing scaling coefficients for the direct arrival signals, M is the number of measurement samples, and N is the number of pixels. The columns of D , d_k , are the discretized version of \tilde{d}_k . The vector g is used to scale each column of D independently.

1.2.3 Joint-MAP Stitching

In order to scan large regions, the sensor assembly is typically moved from one region to another on the surface in raster order to build up a 3D profile of the structure. Typically each scan is individually processed and placed together to present the overall 3D reconstruction, Fig. 1.6. However, this method results in sharp discontinuities at the boundaries and inefficient use of the data collected, Fig. 1.2. We design a joint-MAP technique to solve these issues by modifying the forward model to perform the stitching internally as part of the estimation. This technique is able to remove discontinuities between the sections and make use of any additional information from adjacent scans. Furthermore, the system matrix used in the proposed joint-MAP technique is designed to arrange the small system matrices of single scans in an efficient way to increase the sparsity and reduce the required memory. We assume that adjacent scans share some columns of pixels and have some useful correlations that can be exploited to produce better images. Therefore, the forward model will account for those shared columns differently than the rest of the pixels or columns. For L measurements, we let the system matrix for each measurement be A and the image for each measurement be x_l . We let the order of the pixels in x_l be from top to bottom for each column starting from the far left column to the far right column.

Hence, the term associated with the modified forward model in the MAP estimate will be

$$\frac{1}{2\sigma^2} \|y_{JMAP} - A_{JMAP}x_{JMAP} - D_{JMAP}g_{JMAP}\|^2, \quad (1.8)$$

where

$$A_{JMAP} = \begin{bmatrix} [A] & 0 & 0 & \dots \\ 0 & [A] & 0 & \dots \\ 0 & 0 & [A] & \dots \\ \vdots & \vdots & \vdots & \ddots \end{bmatrix},$$

$$D_{JMAP} = \begin{bmatrix} D & 0 & \dots & 0 \\ 0 & D & \dots & 0 \\ \vdots & \vdots & \ddots & \vdots \\ 0 & 0 & \dots & D \end{bmatrix},$$

$$y_{JMAP} = \begin{bmatrix} y_1 \\ \vdots \\ y_l \\ \vdots \\ y_L \end{bmatrix}, \quad g_{JMAP} = \begin{bmatrix} g_1 \\ \vdots \\ g_l \\ \vdots \\ g_L \end{bmatrix},$$

and x_{JMAP} is the image of the large field-of-view. A_{JMAP} is designed so that if a pixel is shared in more than one image, then its corresponding column in the system matrix for one image will be aligned with its corresponding columns in the system matrix for other images. For the example shown in Fig. 1.6, we can accomplish this alignment by shifting each system matrix A left or right until the required alignment is achieved.

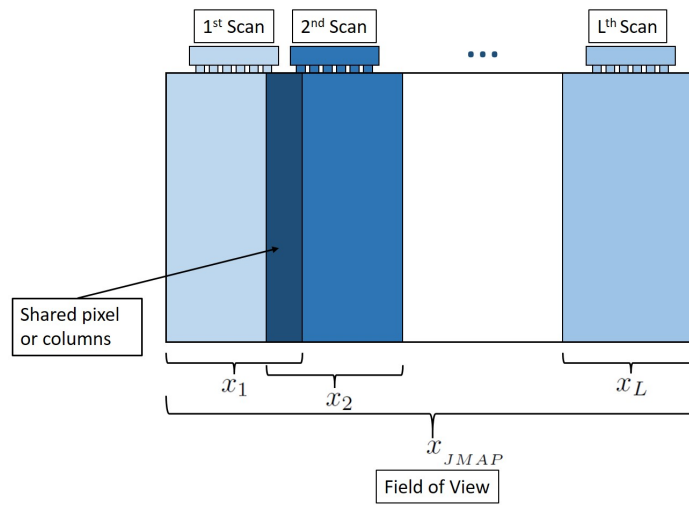


Fig. 1.6. An illustration of multiple measurements needed to scan a large field-of-view. Images from each scan share some pixels with its neighbor images. Proper stitching technique is needed to account for this shared areas in the field-of-view.

1.3 Prior Model Of The Image

We design the prior model of the image to be a combination of a Gibbs distribution and an exponential distribution, i.e.

$$-\log p(x) = \sum_{\{s,r\} \in C} b_{s,r} \rho(x_s - x_r, \sigma_g) + \sum_{s \in S} \frac{x_s}{\sigma_e} + \text{constant},$$

where C is the set of all pair-wise cliques, S is the set of all pixels in the field of view, $b_{s,r}$ is a scaling coefficient, ρ is the potential function, σ_g is the regularization constant for the Gibbs distribution, σ_e is the regularization constants for the exponential distribution, and $x_s \geq 0 \forall s \in S$. We chose the q-generalized Gaussian Markov random field (QGGMRF) as the potential function for the Gibbs distribution [30]. The equation for the QGGMRF is

$$\rho(\Delta, \sigma_g) = \frac{|\Delta|^p}{p\sigma_g^p} \left(\frac{|\frac{\Delta}{T\sigma_g}|^{q-p}}{1 + |\frac{\Delta}{T\sigma_g}|^{q-p}} \right), \quad (1.9)$$

where $1 \leq p < q = 2$ insures convexity and continuity of first and second derivatives, and T controls the edge threshold. The Gibbs distribution is used to preserve edges while the exponential distribution is used to force the background toward zero.

The neighbors of a pixel s are arranged as

$$\begin{bmatrix} r_1 & r_2 & r_3 \\ r_4 & r_5 & r_6 \\ r_7 & r_8 & r_9 \end{bmatrix}, \begin{bmatrix} r_{10} & r_{11} & r_{12} \\ r_{13} & s & r_{14} \\ r_{15} & r_{16} & r_{17} \end{bmatrix}, \begin{bmatrix} r_{18} & r_{19} & r_{20} \\ r_{21} & r_{22} & r_{23} \\ r_{24} & r_{25} & r_{26} \end{bmatrix}. \quad (1.10)$$

where the neighbors with index 10 to 17 are from the same layer, and the rest of the neighbors are from the next and previous layers. With this arrangement, the scaling coefficients $b_{s,r}$ are chosen to be

$$\begin{aligned} \begin{bmatrix} b_{s,r_1} & b_{s,r_2} & b_{s,r_3} \\ b_{s,r_4} & b_{s,r_5} & b_{s,r_6} \\ b_{s,r_7} & b_{s,r_8} & b_{s,r_9} \end{bmatrix} &= \begin{bmatrix} 0 & 0 & 0 \\ 0 & 2 & 0 \\ 0 & 0 & 0 \end{bmatrix} \cdot \frac{\gamma}{4\gamma + 12}, \\ \begin{bmatrix} b_{s,r_{10}} & b_{s,r_{11}} & b_{s,r_{12}} \\ b_{s,r_{13}} & 0 & b_{s,r_{14}} \\ b_{s,r_{15}} & b_{s,r_{16}} & b_{s,r_{17}} \end{bmatrix} &= \begin{bmatrix} 1 & 2 & 1 \\ 2 & 0 & 2 \\ 1 & 2 & 1 \end{bmatrix} \cdot \frac{1}{4\gamma + 12}, \\ \begin{bmatrix} b_{s,r_{18}} & b_{s,r_{19}} & b_{s,r_{20}} \\ b_{s,r_{21}} & b_{s,r_{22}} & b_{s,r_{23}} \\ b_{s,r_{24}} & b_{s,r_{25}} & b_{s,r_{26}} \end{bmatrix} &= \begin{bmatrix} 0 & 0 & 0 \\ 0 & 2 & 0 \\ 0 & 0 & 0 \end{bmatrix} \cdot \frac{\gamma}{4\gamma + 12}, \end{aligned}$$

with a free boundary condition. The parameter γ is set to zero when 2D MBIR is needed, or greater than zero when a 3D regularization (2.5D MBIR) is needed. 2.5D MBIR can be used to gain more information from neighbors of different layers to reduce noise and increase resolution.

1.3.1 Non-linear Spatially-Variant Regularization

The standard form of the regularization introduced above uses constant σ_g and σ_e for all voxels. This can result in reconstruction artifacts because there are few pixels that could have contributed to the signal for closer reflections. However, for deeper reflections, there are many more pixels that could have caused the reflection, i.e. the deeper the reflection the less lateral resolution it has. Fig. 1.7 shows the back-projection of two point scatters of different depth. The closer reflection has less overlapping and higher lateral resolution. The deeper reflection has larger overlapping and lower lateral resolution. This is an issue because MBIR spreads the energy over the intersection area, which attenuates the intensity dramatically for deeper reflections. This smoothing and attenuation appear to increase more rapidly for

deeper reflection. Therefore, a linear spatially-variant regularization as in [13] is not sufficient, and a more generalized model is needed. Hence, we adapt a non-linear spatially-variant regularization technique designed for the UNDE system. We can solve the attenuation problem by assigning less regularization as the pixel gets deeper. The disadvantage of this method is that it will amplify both the reflection and the noise for deeper pixels.

We replace σ_g and σ_e with $\sigma_{g_{s,r}}$ and σ_{e_s} , respectively, where these new parameters are monotone increasing with respect to depth. We assign a new scaling parameter c_s that varies between two values, 1 and c_{\max} , as follows:

$$c_s = 1 + (c_{\max} - 1) * \left(\frac{\text{depth of pixel } s}{\text{maximum depth}} \right)^a \quad (1.11)$$

where $a > 0$ and $c_{\max} > 1$. Then, $\sigma_{g_{s,r}}$ and σ_{e_s} are calculated as follows:

$$\begin{aligned} \sigma_{g_{s,r}} &= \sigma_g \sqrt{c_s c_r}, \\ \sigma_{e_s} &= \sigma_e c_s, \end{aligned}$$

where c_r has the same equation as in c_s , but for pixel r.

1.3.2 Selection of Prior Model Parameters

The selection of the prior model parameters is an open area of research. In this thesis, we select the regularization parameters σ_g , σ_e and γ (which control edge preservation, background sparsity, and contribution from neighbors of adjacent layers, respectively) to produce the best results visually. The parameters p , q , T , and a (which controls the transitioning from high to low regularization as the pixels get deeper) are unitless parameters and the values used for them in this thesis are considered standard and seem to be consistent with the applications we are working on. The parameter c_{\max} is a unitless parameter and is used to amplify reflections for deeper regions as needed.

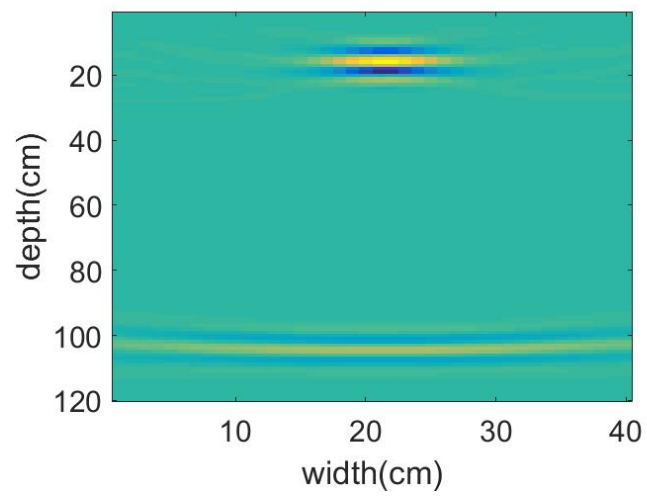


Fig. 1.7. Back-projection of two point scatterers, one that is closer to the transducers (17cm deep) and one that is far from the transducers (105 cm deep). As the reflection gets deeper, the lateral resolution decreases.

1.4 Optimization of MAP Cost Function

After designing the forward model and the prior model, the MAP estimate becomes

$$\begin{aligned}
(x, g, \sigma^2)_{MAP} = \arg \min_{x \geq 0, g, \sigma^2} & \left\{ \frac{1}{2\sigma^2} \|y - Ax - Dg\|^2 \right. \\
& + \frac{MK}{2} \log(\sigma^2) + \sum_{\{s,r\} \in C} b_{s,r} \rho(x_s - x_r, \sigma_{g_{s,r}}) \\
& \left. + \sum_{s \in S} \frac{x_s}{\sigma_{e_s}} \right\}. \tag{1.12}
\end{aligned}$$

The shifting of the direct arrival signal matrix D mentioned in section 1.2.1 is performed once before estimating g , x and σ^2 . The solution for g is straightforward:

$$\begin{aligned}
0 &= \nabla_g \left\{ \frac{1}{2\sigma^2} \|y - Ax - Dg\|^2 + \frac{MK}{2} \log(\sigma^2) \right. \\
& \quad \left. + \sum_{\{s,r\} \in C} b_{s,r} \rho(x_s - x_r, \sigma_{g_{s,r}}) + \sum_{s \in S} \frac{x_s}{\sigma_{e_s}} \right\} \\
\implies 0 &= 2D^t Dg + 2D^t Ax - 2D^t y \\
\implies g &= (D^t D)^{-1} D^t (y - Ax).
\end{aligned}$$

Given x , the evaluation of g is computationally inexpensive because $D^t D$ is a diagonal matrix, i.e.

$$(D^t D) = \begin{bmatrix} d_1^t d_1 & 0 & \dots & 0 \\ 0 & d_2^t d_2 & \dots & 0 \\ \vdots & \vdots & \ddots & \vdots \\ 0 & 0 & \dots & d_K^t d_K \end{bmatrix},$$

where d_k is the discretized version of $\tilde{d}_k(t)$ for transducer pair k . However, g requires the knowledge of x which is the image we would like to reconstruct. This issue can

be resolved by updating the value of g from the updated image in each iteration. Furthermore, for each iteration, we update g , x , and σ^2 in the following steps:

$$\begin{aligned} g &\leftarrow (D^t D)^{-1} D^t (y - Ax) \\ y &\leftarrow y - Dg \\ x &\leftarrow \arg \min_{x \geq 0} \left\{ -\log p(y|x) - \log p(x) \right\} \\ \sigma^2 &\leftarrow \frac{1}{MK} \|y - Ax\|^2 \end{aligned}$$

We adopt the iterative coordinate descent (ICD) technique to optimize the cost function with respect to x [31]. Since the prior model term is non-quadratic, optimizing the cost function will be computationally expensive. Therefore, we use the surrogate function (majorization) approach with ICD to resolve this issue [30]. This ICD optimization algorithm is guaranteed to converge to the global minimum because the function being minimized is continuously differentiable and strictly convex [30]. Fig. 1.8 shows the complete algorithm for ICD using the majorization approach. The algorithm is stopped either if

$$\frac{\|x_{n-1} - x_n\|}{\|x_{n-1}\|} < \epsilon, \quad (1.13)$$

where x_n is the current image update and ϵ is a stopping threshold, or if the number of iterations exceeds a specified number, e.g. 100 iterations. Empirically, we have found that a value of $\epsilon = 0.01$ is a sufficient value to declare convergence with zero initialization.

1.5 Results

In this section we compare MBIR with two different techniques qualitatively and quantitatively.

ICD Algorithm Using Majorization Technique

Initialize x , $e \leftarrow y - Ax$, σ^2

For $p = 1$: Number of transducer pairs{

$n_p = \arg \max_{n_p} \{y_p^t d_p(n - n_p)\}$

$d_p \leftarrow d_p(n - n_p)$

}

Repeat if stopping condition is not met {

$g = (d^t d)^{-1} d^t e$

$e \leftarrow e - dg$

For each pixel $s \in S$ {

$\tilde{b}_{s,r} \leftarrow \frac{b_{s,r} \rho'(x_s - s_r)}{2(x_s - x_r)}$

$\theta_1 \leftarrow -\frac{e^t A_{*,s}}{\sigma^2} + \sum_{r \in \partial s} 2\tilde{b}_{s,r}(x_s - x_r)$

$\theta_2 \leftarrow \frac{A_{*,s}^t A_{*,s}}{\sigma^2} + \sum_{r \in \partial s} 2\tilde{b}_{s,r}$

$\alpha^* \leftarrow \text{clip} \left\{ \frac{-\theta_1}{\theta_2}, [-x_s, \infty) \right\}$

$e \leftarrow e - A_{*,s} \alpha^*$

$x_s \leftarrow x_s + \alpha^*$

}

$\sigma^2 \leftarrow \frac{\|e\|^2}{MK}$

}

Fig. 1.8. ICD algorithm using the majorization technique with shift error estimation (top red box) and direct arrival modeling (bottom red box) [30, 31].

1.5.1 Algorithms for Comparison

We compare MBIR with the SAFT and l_1 -norm techniques. The l_1 -norm is a regularized iterative technique with the same forward model as in Eq. 1.5 with an exponential distribution prior. The prior model is exactly equal to an l_1 regularization term with a positivity constraint. The MAP estimate for the l_1 -norm technique is

$$(x, \sigma^2)_{MAP} = \arg \min_{x \geq 0, \sigma^2} \left\{ \frac{1}{2\sigma^2} \|y - Ax\|^2 + \frac{MK}{2} \log(\sigma^2) + \sum_{s \in S} \frac{x_s}{\sigma_{e_s}} \right\}. \quad (1.14)$$

A pixel-wise precision-recall (PR) plot is used for the simulated data to compare the performance of the techniques qualitatively. A pixel-wise PR test calculates the number of true positive (TP), false positive (FP), and false negative (FN) for each technique. These values are used to plot the precision vs. recall (PR) curves where

$$recall = \frac{TP}{TP + FN}$$

and

$$precision = \frac{TP}{TP + FP}.$$

This detection test compares the performance of each technique by the area under the PR curve. The larger the area the better the technique. Next, for each technique, all the images are normalized by dividing them with their maximum value. Thresholds from 1 to 0 with step 0.001 are applied to all images. For each threshold, a TP is declared if the defect diagram (ground truth) pixel is 1 and the reconstructed pixel is 1. A FP is declared if the defect diagram pixel is 0 and the reconstructed pixel is 1. A FN is declared if the defect diagram pixel is 1 and the reconstructed pixel is 0.

The techniques performance for the simulated data will be compared with measurements of different signal-to-noise ratio (SNR). The SNR is defined as

$$SNR = \frac{\|y\|^2}{\|w\|^2},$$

where y is the noiseless simulated output from k-wave, and w is the added noise to y .

A component-wise PR plot is used for the experimental data to compare the performance of each technique. Each image is segmented into connected components using the standard Matlab functions “edge” and “imfill”. Next, the maximum value and weighted centroid for each connected component is stored. Next, a search is performed pairing targets from the defect diagram to connected components from the reconstruction in the following way: A connected component is mapped to a particular target if its centroid is both the closest among all detected components to the target’s centroid, and it is within 10 cm of the target’s centroid. Next, for each technique, all the images are normalized by dividing them with the maximum value of them all. Thresholds from 1 to 0 with step 0.001 are applied to all images. For each threshold, a TP is declared if the maximum value of a paired connected component is equal or greater than the threshold. A FP is declared if the maximum value of an unpaired connected component is equal or greater than the threshold. The FN is calculated by subtracting the number of TP’s from the number of targets.

A normalized root mean square error (NRMSE) plot will be used to compare MBIR convergence with different initializations. The NRMSE is defined as

$$NRMSE(n) = \frac{\|X_n - X_{true}\|}{\|X_{true}\|}, \quad (1.15)$$

where n is the iteration number, and X_{true} is the true solution. We define X_{true} to be iteration 1500 of the zero initialization.

1.5.2 K-wave Simulated Results

The k-wave simulator has been used to simulate acoustic propagation through concrete medium [32]. The concrete structure was embedded with steel of different shapes. The width and depth of the structure is 40cm and 30cm , respectively. 10 transducers were used to transmit and receive. For each simulation, the simulator produces 90 outputs from all pairs of transducers where only distinct pairs are used, i.e. 45 distinct pairs. The transducers are placed at the top center of the field-of-view and separated by 4cm from each other. To simulate the acoustic propagation using

k-wave, we provided three images of speed, density, and attenuation as inputs to k-wave. Each pixel in the three input images corresponds to the characteristics of either steel or cement. The output of k-wave is then used as input to the reconstruction methods. Fig. 1.9 shows reconstruction results for four different tests. The voxel spacing for 2D reconstructions is 1 cm for all reconstruction techniques. The left column shows the designed defect diagram that was used for simulation where the white pixels corresponds to cement and the black pixels corresponds to steel. The next column shows the instantaneous envelope of SAFT reconstruction. The next column is l_1 -norm. The right column shows the MBIR reconstruction. Both l_1 -norm and MBIR were initialized to zero. Note that SAFT does not share the same unit with MBIR or L1-norm. That is why it shows different scaling.

Fig. 1.11 shows the pixel-wise PR curve for each technique over all 4 tests. Table 1.4 shows values of the area under the PR curves in Fig. 1.11. Table 1.1 shows the parameters which are used for k-wave simulation, and some of them are used as input parameters in all techniques. Table 1.3 shows the parameters used for l_1 -norm and MBIR in Eq. 1.1, 1.9, and 1.11, and the stopping threshold.

Fig. 1.10 shows a comparison between the methods with noise added to the simulated signal of the defect diagram of Test 1 in Fig. 1.9.

Discussion

In Fig 1.9, MBIR and l_1 -norm were able to show significant enhancement over SAFT in reducing noise. MBIR showed remarkable performance in identifying, eliminating, and distinguishing the direct arrival signal artifacts from the steel objects. For example, in test 1, two steel plates where placed at depth 2cm. The plates where overshadowed by the direct arrival signal artifacts in SAFT and l_1 -norm, but appear very clearly in MBIR. Test 2 and 3 also show similar direct arrival signal overshadowing effects for SAFT and l_1 -norm, that are reduced for MBIR. In addition, the steel objects are more easily observed and recognized in l_1 -norm and MBIR. In Fig. 1.11

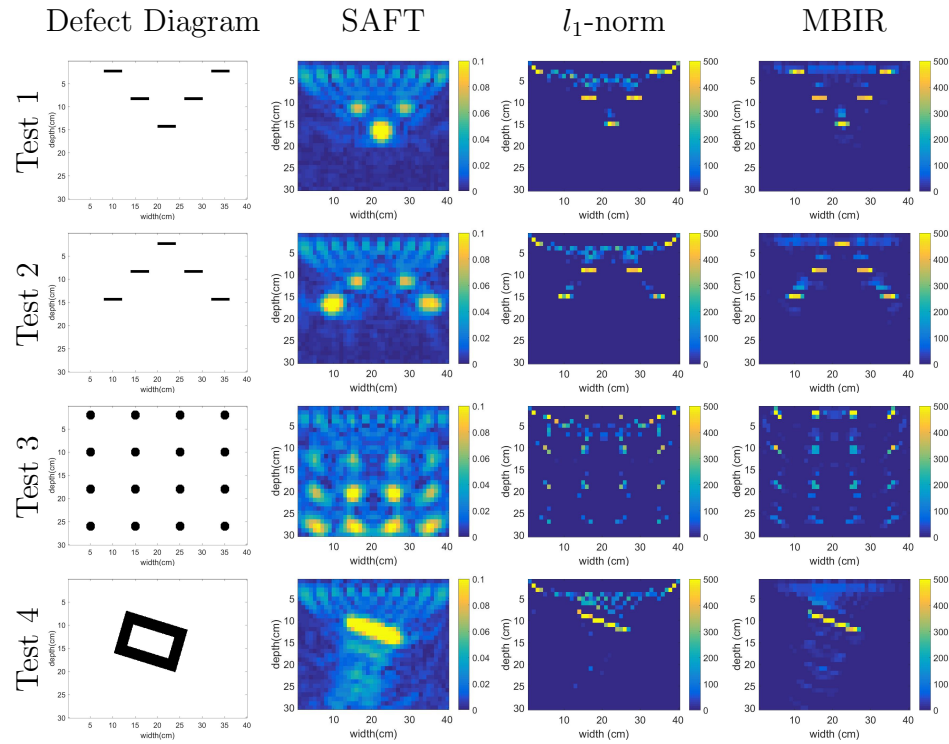


Fig. 1.9. Comparison between MBIR and SAFT reconstruction from the k-wave simulated data. The far left column is the position of the defects. The next column is SAFT reconstruction. The next column is l_1 -norm reconstruction. The far right column is MBIR reconstruction. MBIR tends to produce results with less noise and artifacts compared to SAFT and l_1 -norm.

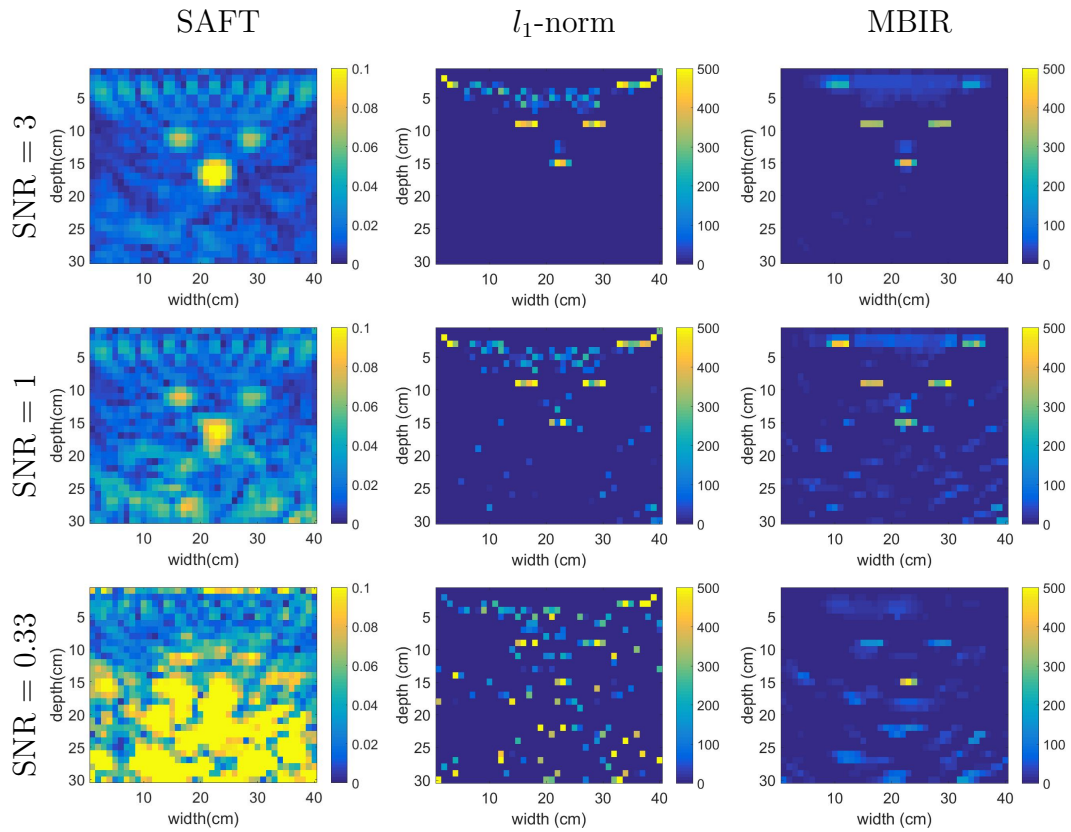


Fig. 1.10. Comparison between SAFT, l_1 -norm, MBIR reconstructions from the k-wave simulated data with different SNR. The defect diagram is the same as the defect diagram in Test 1 in Fig. 1.9. The left column is SAFT reconstruction. The next column is l_1 -norm reconstruction. The right column is MBIR reconstruction. Each row correspond to different SNR value where the SNR values from top to bottom are 3, 1, and 0.33, respectively. MBIR tends to produce results with less noise and artifacts compared to SAFT and l_1 -norm.

Table 1.1.
Parameter settings for k-wave simulation.

Parameters	Value	Unit
Carrier frequency	52	kHz
Sampling frequency	1	MHz
Cement speed	3680	m/s
Cement density	1970	Kg/m^3
Cement attenuation	1.46e-6	$dB/((MHz)^y cm)$
Steel speed	5660	m/s
Steel density	8027	Kg/m^3
Steel attenuation	4.85e-8	$dB/((MHz)^y cm)$
Spatial resolution	1	mm
Number of columns	400	-
Number of rows	300	-
Number of transducers	10	-

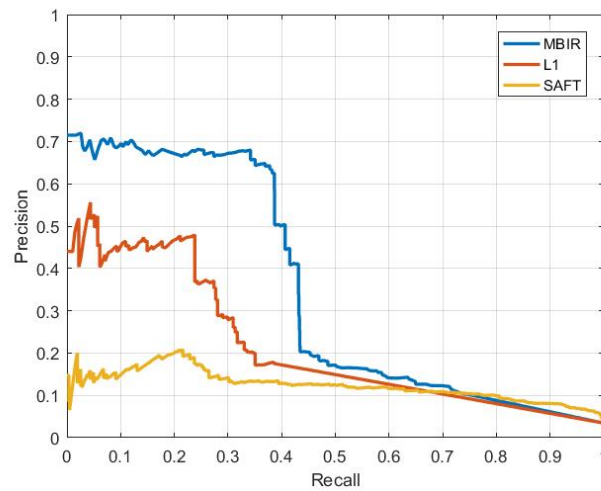


Fig. 1.11. PR curves for each technique over all 4 tests in Fig.1.9. MBIR outperforms the other techniques by having the highest PR area.

and Table 1.4, MBIR shows better performance in the detection test with the highest PR area.

Notice that in test 4, none of the techniques were able to show the complete structure of the steel object. They were able to show only one side of it. This is because all three reconstruction methods reconstruct the reflections caused by discontinuous boundaries rather than recovering the actual material property at each voxel location.

Fig. 1.10 shows the reconstruction of test 1 in Fig. 1.9 with varying signal-to-noise ratio (SNR). As the SNR decreases, the reconstruction becomes noisier for all techniques. However, the results show better performance in MBIR than the other techniques in reducing noise and artifacts.

1.5.3 MIRA Experimental Results

Experimental results have been obtained from a designed thick concrete specimen [33]. The height and width of the specimen is 213.36 cm (84 inches), Fig. 1.12. The depth of the specimen is 101.6 cm (40 inches). Each side of the block is gridded with 10.16 cm squares producing 21 rows and columns. The specimen has been heavily reinforced with steel rebars horizontally and vertically with 1 ft separation in both sides. One side is “smooth” and the other is “rough” which refer to the physical characteristic of the concrete surface due to pouring. Also, Fig. 1.14 and Fig. 1.15 show diagrams of the steel rebars in green color with more details. The specimen has been embedded with designed defects placed in specific locations. The type and location of the defects are shown in Figs. 1.13, 1.14, 1.15, and 1.16 [33]. The specified location of the defects might be different from the real location due to possible displacement while pouring the cement.

The defects are designed to simulate real defects that can occur due to construction process, cumulative deterioration, or degradation of concrete. Four datasets were obtained by scanning both sides horizontally and vertically: smooth-horizontal, smooth-vertical, rough-horizontal, and rough-vertical. Each dataset contains 17 to

19 cross-sections or slices of the specimen which adds up to 73 cross-sections. Each cross-section is scanned 18 times from different positions to cover the entire field of view. The first and last scans are centered at 20.32 cm (8 inches) from the edge. The rest of the scans are spread evenly by a 10.16-cm (4-inch) separation, hence the 18 scans.

The MIRA system has been used to collect the data [34]. The MIRA device, Fig. 1.12, contains 10 columns or channels separated by 40 mm where each channel contains 4 dry contact points with 2 mm radius that act as transmitters or receivers. Only the 45 distinct pairs are used in the reconstruction results for all techniques. The transmitter emits a signal with a carrier frequency of 52 kHz, and the sampling frequency of the receiver is 1 MHz. The acoustic speed is assumed to be $2620 \frac{m}{s}$. Each distinct pair produces 2048 samples of data where the first 27 samples are ignored due to trigger synchronization. The data is then down-sampled to 200 kHz and 409 samples and reconstructed using all techniques.

Four different techniques were used to reconstruct the data: SAFT, l_1 -norm, 2D MBIR, and 2.5D MBIR. Zero initialization was used for l_1 -norm, 2D MBIR, and 2.5D MBIR. For SAFT, the multiple scans are jointly reconstructed to avoid stitching artifacts. For l_1 -norm, all scans for each cross-section are reconstructed individually and then stitched together. For 2D MBIR and 2.5D MBIR, the joint-MAP stitching is used to reconstruct the entire cross-section.

Fig. 1.17 shows the reconstruction results. The field of view of each cross-section is 120×210 cm and the reconstruction resolution is 1 cm for all techniques. The first row shows the defect diagram and the position of the defects. The second row is the instantaneous envelope of SAFT reconstruction. The third row is l_1 -norm reconstruction. The fourth row is 2D MBIR reconstruction. The fifth row is 2.5D MBIR reconstruction. Note that the defect diagram shows the steel rebars as dotted circles or dotted rectangles. The steel rebars might appear in all reconstructions as small horizontal dots or a horizontal line at the top, but the bottom steel rebars barely appear in all techniques due to their weak reflection. Table 1.2 shows the

common parameter settings for all techniques. Table 1.3 shows the l_1 -norm and MBIR parameter settings for Eq. 1.1, 1.9, and 1.11, γ in section 1.3, and the stopping threshold.

Fig. 1.18 shows the PR curve for each technique over the four datasets. Since the position of the targets in the defect diagram is not precise, the detection test was done using the component wise approach rather than the pixel-wise approach used for the k-wave data. To make a fair comparison, the parameter σ_g for MBIR, the parameter σ_e for l_1 -norm, and the parameters σ_g and γ for 2.5D MBIR were chosen using a grid search to maximize the area under the PR curves. Table 1.4 shows the value of the area under the PR curves in Fig. 1.18.

All the techniques were implemented in Linux using a 2.60GHz Sky Lake CPU. SAFT, l_1 -norm, 2D MBIR, and 2.5D MBIR processed the four datasets which consist of 73 slices of size 120×210 pixels in approximately 1, 28, 23, and 30 minutes, respectively.

Discussion

In Fig. 1.17, MBIR shows significant enhancement in reducing artifacts and reducing noise compared with SAFT and l_1 -norm. SAFT and MBIR techniques were able to show the back wall of the specimen. The back wall is located at depth 100 cm. The detection test showed better performance of 2.5D and 2D MBIR over all techniques with 2.5D MBIR being slightly better than 2D MBIR.

Since all three algorithms are based on a linear forward model, they all exhibit certain reconstruction artifacts such as multiple reflection echos of a single defect. For example, multiple echos appeared of defect 13 in smooth-ver-slice8 for all techniques.



Fig. 1.12. The concrete specimen and the MIRA device used for the experimental data [33]. 20 defects are embedded in the specimen.

Table 1.2.

Parameter settings used for all techniques to reconstruct the experimental MIRA data.

Parameters	Value	Unit
Carrier frequency	52	<i>kHz</i>
Sampling frequency	200	<i>kHz</i>
Cement p-wave speed	2620	<i>m/s</i>
Reconstruction resolution	1	<i>cm</i>
Number of columns	210	-
Number of rows	120	-

DEFECT TABLE		
ID NUMBER	DESCRIPTION	LABEL
D1	POROUS HALF CYLINDER (NO COVER)	
D2	POROUS HALF CYLINDER (COVER)	
D3	POROUS HALF CYLINDER (NO COVER)	
D4	POROUS HALF CYLINDER (COVER)	
D5	POROUS HALF CYLINDER (COVER & CRACK)	
D6	PVC	
D7	PVC	
D8	DISSOLVING STYROFOAM (THICK)	
D9	STYROFOAM (THICK)	
D10	STYROFOAM (THIN)	
D11	PLEXIGLASS	
D12	DISSOLVING STYROFOAM (MEDIUM)	
D13	STYROFOAM (MEDIUM)	
D14	PLEXIGLASS	
D15	DISSOLVING STYROFOAM (THIN)	
D16	LUMBER (2X4)	
D17	GLOVES	
D18	DEBOND DUCT TAPE (ONE LAYER)	
D19	DEBOND DUCT TAPE (MULTI-LAYER)	
D20	MOVING REBAR	

Fig. 1.13. Type and legend for each defect [33]. These defects are embedded in the concrete specimen.

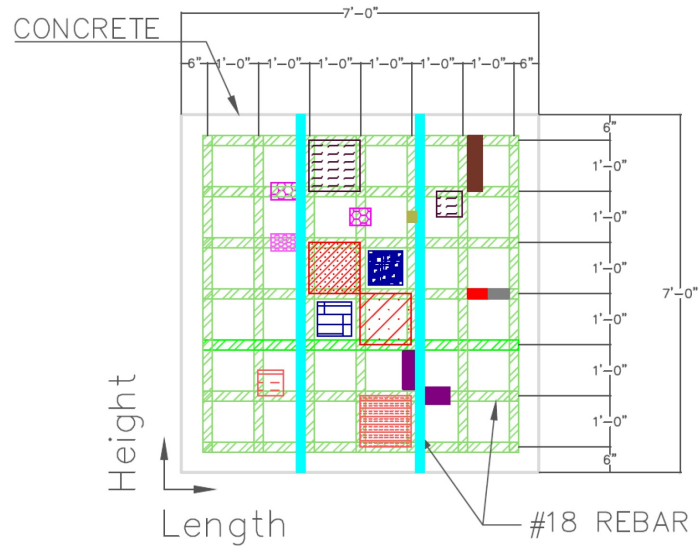


Fig. 1.14. Smooth side view of defects [33]. The location of the defects is approximated due to possible displacement while pouring the cement.

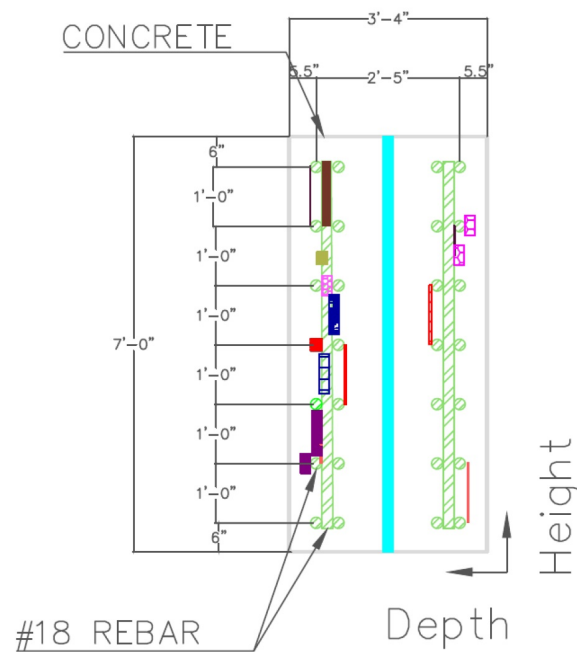


Fig. 1.15. Depth view of defects, smooth side on the right and rough side on the left, [33]. The location of the defects is approximated due to possible displacement while pouring the cement.

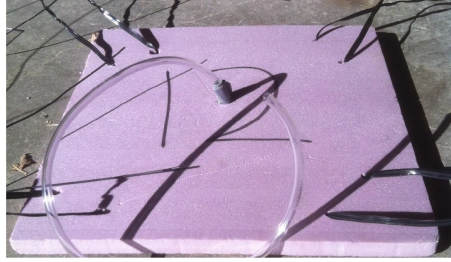


Fig. 1.16. A picture of defect 12 before embedding it in the specimen, [33]. It is made of dissolving styrofoam.

Table 1.3.

The l_1 -norm, 2D MBIR, and 2.5D MBIR parameter settings used in the simulated K-wave and the experimental MIRA data.

Parameters	l_1 -norm	2D MBIR	2.5D MBIR	Unit
ϵ	0.01	0.01	0.01	-
α_0	30	30	30	$(MHz \cdot m)^{-1}$
p	-	1.1	1.1	-
q	-	2	2	-
T	-	1	1	-
c_{max}	-	10	10	-
a	-	3	3	-
σ_g	-	3	3	m^{-3}
σ_e	15	15	15	m^{-3}
γ	-	-	0.5	-

Table 1.4.

Precision vs recall area for all techniques in Fig. 1.11 and Fig. 1.18. MBIR has the highest PR area.

	SAFT	l_1 -norm	2D MBIR	2.5D MBIR
PR area for k-wave data	0.1236	0.2131	0.3476	-
PR area for MIRA data	0.1397	0.1932	0.2836	0.2908

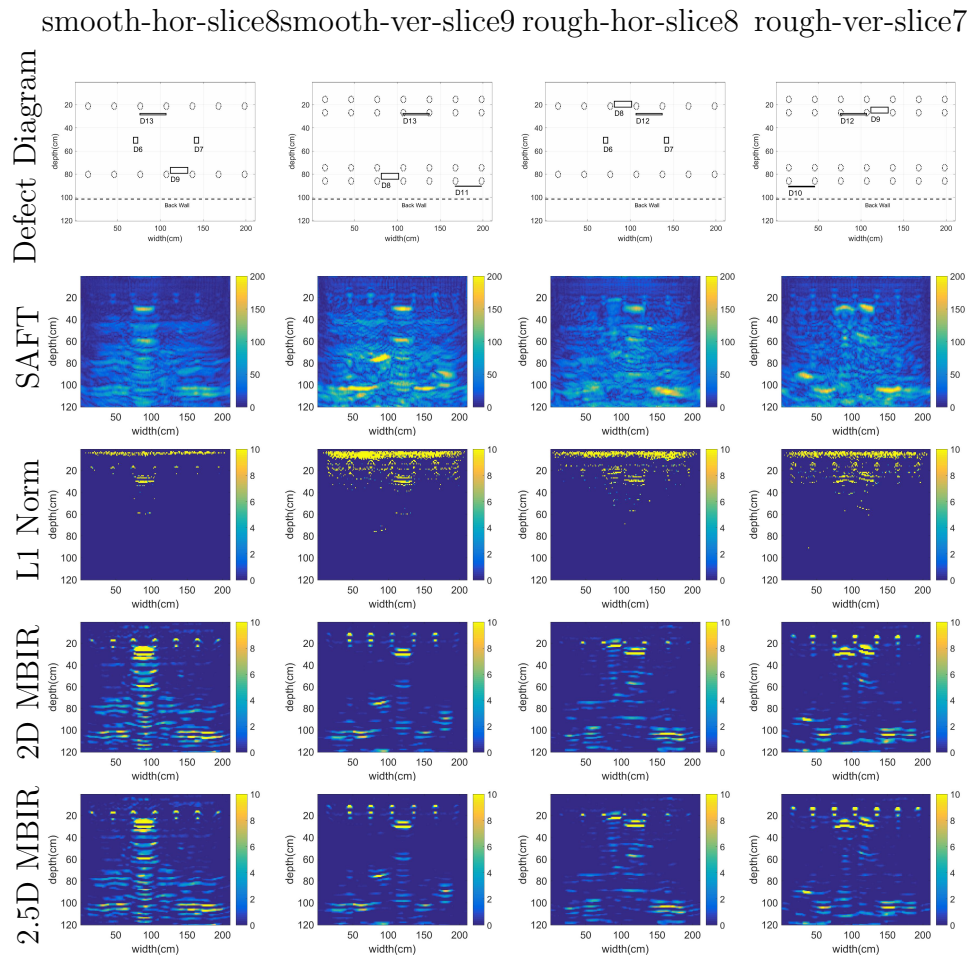


Fig. 1.17. Comparison between all reconstruction results from the MIRA experimental data: the first row from the top is the position of the defects, the second row is SAFT reconstruction, the third row is l_1 -norm reconstruction, the fourth row is 2D MBIR reconstruction, and the fifth row is 2.5D MBIR reconstruction. 2.5D and 2D MBIR tend to produce results with less noise and artifacts compared to other techniques.

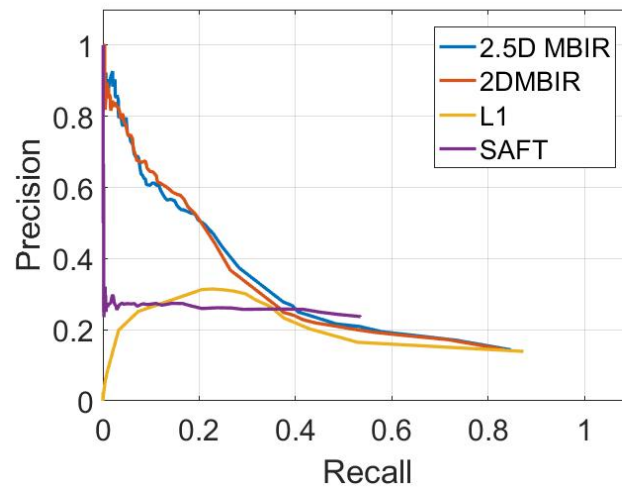


Fig. 1.18. PR curves for each technique over all 73 slices in the MIRA experimental data. 2.5D and 2D MBIR outperforms the other techniques.

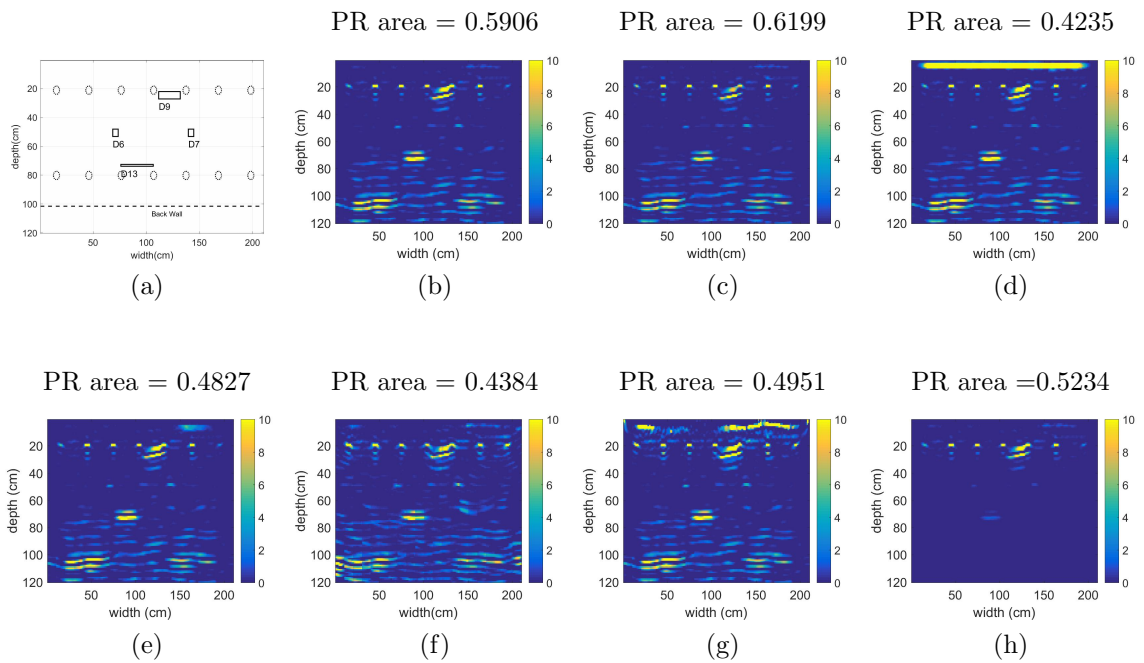


Fig. 1.19. A comparison between different settings of MBIR where (a) is the defect diagram of rough-hor-slice11, (b) is 2D MBIR reconstruction, (c) is 2.5D MBIR reconstruction with all modifications to the forward and prior models, (d) is 2D MBIR reconstruction without direct arrival signal or shift error estimation, (e) is 2D MBIR reconstruction without shift error estimation, (f) is 2D MBIR reconstruction using regular stitching, (g) is 2D MBIR reconstruction using an isotropic model, (h) is 2D MBIR reconstruction for a constant regularization. The results in (c) shows performance enhancement over the other results.

1.5.4 Results from Modifying the Forward and Prior Models

In this section, we investigate the effect of various MBIR model attributes on the image quality resulting from the MIRA data reconstructions. In particular, we computed reconstructions *without* direct arrival signal elimination, shift error estimation, anisotropic reconstruction, and spatially variant regularization. We then compared each of these degraded results to the baseline MBIR reconstructions using the complete MBIR algorithm in order to better understand the value of each technique in overall image quality. We also calculated the component-wise PR area for each reconstruction.

Fig. 1.19 compares MBIR performance when not using each modification. Fig. 1.19b shows 2D MBIR reconstruction with PR area = 0.5906. Fig. 1.19c shows 2.5D MBIR reconstruction with PR area = 0.6199. Fig. 1.19d shows 2D MBIR reconstruction without the direct arrival signal modeling with PR area = 0.4235. Fig. 1.19e shows 2D MBIR reconstruction with the direct arrival signal modeling, but not the shift error estimation, with PR area = 0.4827. Fig. 1.19f shows 2D MBIR reconstruction with regular stitching with PR area = 0.4384. Fig. 1.19g shows 2D MBIR reconstruction with an isotropic forward model with PR area = 0.4951. Fig. 1.19h shows 2D MBIR reconstruction with constant regularization with PR area = 0.5234. All the PR areas specified in Fig. 1.19 were obtained by calculating the precision and recall for each plot for only the cross-section shown in Fig. 1.19a.

Discussion

Fig. 1.19d does not model the direct arrival which causes the reconstruction to have artifacts at the top of the image. These artifacts have high amplitude and could overshadow targets closer to the transducers. Fig. 1.19e reduces these artifacts by modeling the direct arrival signal. However, some residual of the artifacts still appears at the top right corner due to changes in acoustic speed in the concrete medium. Fig. 1.19f shows the results of performing conventional stitching technique

to stitch the reconstruction from multiple scans. The stitching method produces vertical discontinuities at the boundaries between the stitched images. Also, the stitching method does not make use of additional information that can be obtained from adjacent scans to improve the reconstruction. Fig. 1.19g uses an isotropic model for the transmitted beam which produces artifacts at the top of the image. These artifacts appear because of the assumption that the signal travels in all directions equally which allows MBIR to use pixels with large transmitter-pixel or pixel-receiver angles to fit the data. Fig. 1.19h uses a spatially constant regularization which suppresses weak details in deep regions of the reconstruction. This results from the fact that the signal is dramatically attenuated as it propagates into deeper regions. Consequently, reconstruction with a constant regularization attenuates most useful detail in the deep parts of the image.

In contrast, Fig. 1.19b shows 2D MBIR with much better performance in reducing artifacts, exploiting correlations from adjacent scans, showing targets for deeper regions, and having larger PR area. Finally, Fig. 1.19c shows the 2.5D MBIR reconstruction which is qualitatively and quantitatively slightly better than 2D MBIR.

1.5.5 Convergence of MBIR

To show the algorithm's convergence behavior, we reconstructed cross-section rough-hor-slice11 in Fig. 1.19a from the MIRA data with different initializations: uniformly distributed random noise with range $[0, 10]$, zero, a constant value of 10. Fig. 1.20 shows the NRMSE vs. iteration for the different initializations.

1.6 Summary

This thesis proposed an MBIR algorithm for ultrasonic one-sided NDE. The thesis showed the derivation of a linear forward model. The QGGMRF potential function for the Gibbs distribution prior model was chosen for this problem because it guarantees function convexity, models edges and low contrast regions, and has continuous first

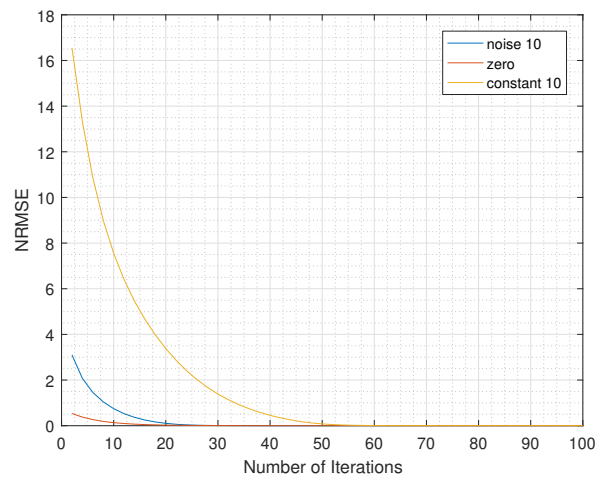


Fig. 1.20. NRMSE vs. iteration for different initializations in the MBIR algorithm. The initializations used in the plot are uniformly distributed random noise with range $[0, 10]$, zero, and a constant value of 10, respectively.

and second derivatives. Furthermore, we proposed modifications to both the forward and prior models that improved reconstruction quality. These modifications included direct arrival signal elimination, anisotropic transmit and receive pattern, and spatially variant regularization. Additionally, a joint-MAP estimate and a 2.5D MBIR were performed to process large multiple scans at once which helps reduce noise and artifacts dramatically compared with results from individual scans. The research was supported by simulated and extensive experimental results. The results compared the performance of MBIR with SAFT and l_1 -norm qualitatively and quantitatively. The results showed noticeable improvements in MBIR over SAFT and l_1 -norm in reducing noise and artifacts.

While the results of this thesis are promising, it is worth mentioning the need of a non-linear forward model to address the issues due to the complexity of the one-sided UNDE systems, such as reverberation, and acoustic shadowing.

2. DIRECT DEEP LEARNING FOR ONE-SIDED ULTRASONIC NON-DESTRUCTIVE EVALUATION

2.1 Introduction

One-sided ultrasound non-destructive evaluation (UNDE) is vital for inspecting large heterogeneous specimens, such as the casing of injection wells and thick concrete walls [35]. To perform the inspections, different kind of systems are used to extract ultrasonic data, such as plane wave imaging (PWI) [36,37] and multi-static array [34]. In a PWI system, all the transducers transmit at the same time and receive the reflections. In a multi-static array system, each transducer transmits individually while the rest of the transducers receive (see Fig. 2.1). PWI is typically used for real time reconstruction while multi-static array system is more preferred in some applications, such as inspecting large concrete structures, to acquire more information. However, raw data from multi-static array cannot be arranged to form an image with simple continuous patterns or artifacts as in PWI, Fig. 2.2, which requires post-processing to reconstruct an image with much simpler artifacts.

Due to the need for rapid reconstructions with multi-static array, full waveform inversion approaches [38] are not practical for ultrasound NDE and hence analytic algorithms based on a delay-and-sum approach, such as the synthetic aperture focusing technique (SAFT), are routinely used for reconstructions of ultrasound reflection mode data [8–10].

Recently, we have developed a model-based iterative reconstruction [39] approach using a simplified linear model and demonstrated significant improvements in reconstructed image quality as compared to SAFT, while still being able to produce a reconstruction in near real-time. However, this MBIR method still results in artifacts

due to the inherent non-linearity of the ultrasound system. In summary, existing approaches for one-sided UNDE may result in reconstructions with significant artifacts.

There have been several recent efforts to use deep convolutional neural networks (CNN) to address inverse problems in imaging [40]. One class of algorithms applies a two-step, non-iterative approach composed of a simple inversion followed by a CNN to obtain a reconstruction for inverse problems such as tomography [41, 42], MRI [43, 44], photo-acoustic tomography [45, 46], compressed sensing [47], and non-linear optical imaging based on multiple scattering [48]. Alternatively, researchers have adapted variable splitting strategies such as the Plug-and-Play approach [49, 50] to iteratively solve two *learned* sub-problems corresponding to a forward-model inversion and a denoising step [46, 51–55]. In summary, deep-learning based techniques have demonstrated promising results for a variety of inverse problems in imaging.

Recently, methods have been proposed for non-iterative reconstruction of PWI ultrasound data using CNNs [56, 57]. In this approach, the CNN can directly process the ultrasound data because the PWI ultrasound data can be arranged to form an image with simple patterns that the CNN can sufficiently model. However, this approach is not directly applicable to the reconstruction of multi-static UNDE data.

In this thesis, we present a direct deep learning (DDL) method for reconstructing high-quality images from multi-static one-sided ultrasound data. Our method is based on a two-step process. In the first step, we transform the raw data from the measurement domain to the image domain using a simple linear back-projection. In the second step, we use a multi-scale deep convolutional neural network to compute the final reconstructed image. In addition, we propose methods for training the algorithm from ultrasound simulation data that make it robust to model mis-match and compensate for the attenuation of deeper reflections.

Furthermore, we compare the results of our proposed DDL algorithm to the reconstructions produced by SAFT and MBIR using both simulated and real data, and we demonstrate qualitative reductions in noise and artifacts along with quantitative improvements in precision-recall performance on ground-truth targets.

We introduce five major contributions in this thesis:

- 1) A non-iterative two-stage inversion approach using back-projection and CNN for multi-static UNDE applications;
- 2) An approach to reducing modeling mismatch effects when reconstructing from real data;
- 3) A space-variant amplification approach for more accurate reconstruction of deep targets;
- 4) A joint CNN technique for the reconstruction of multiple multi-static scans for large field-of-view imaging;
- 5) Qualitative and quantitative results from simulated and experimental data.

The organization of the rest of this thesis is as follows. In section 2.2, we cover the ultrasound forward model. In section 2.3, we cover our proposed technique. In section 2.4, we cover the modeling mismatch issue. In section 2.5, we cover the attenuation of deeper region issue. In section 2.6, we cover the joint reconstruction approach. Finally, in section 2.7, we cover results from simulated and experimental data.

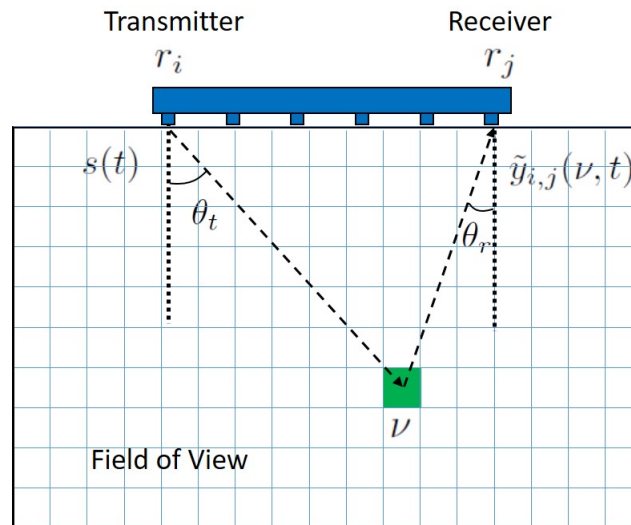


Fig. 2.1. Illustration of a widely used ultrasound system for one-sided non-destructive evaluation using a multi-static array. The transducers are used to make pulse-echo measurements which are processed to reconstruct the cross-section.

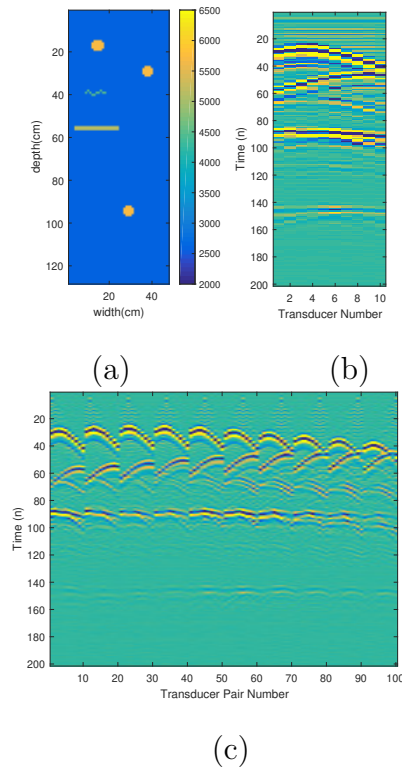


Fig. 2.2. Illustration of raw data (arranged to form a 2D image) obtained from PWI and multi-static array using 10 transducers. (a) is the ground truth image. (b) is the raw data obtained from PWI where each column correspond to the received signal at one transducer. (c) is the raw data obtained from multi-static array where each column corresponds to one transmit-receive pair.

2.2 Ultrasound Forward Model and Linear Model-Based Inversion

The goal of ultrasound reflection mode imaging is to determine the properties of a cross-section being imaged using a transducer array (See Fig. 2.1). In particular,

the ultrasound wave propagation in a medium can be described by a set of coupled partial differential equations [58],

$$\begin{aligned}\frac{\partial u}{\partial t} &= -\frac{1}{\rho_0}\nabla p, \\ \frac{\partial \rho}{\partial t} &= -\rho_0\nabla u - u\nabla\rho_0, \\ p &= c_0^2(\rho + d \cdot \nabla\rho_0 - L\rho),\end{aligned}\tag{2.1}$$

where u is the acoustic particle velocity, ρ is the acoustic density, d is the acoustic particle displacement, L is an operator defined by

$$L = -2\alpha_0 c_0^{y-1} \frac{\partial}{\partial t} (-\nabla^2)^{\frac{y}{2}-1} + 2\alpha_0 c_0^y \tan\left(\frac{\pi y}{2}\right) (-\nabla^2)^{\frac{y+1}{2}-1},$$

and $0 < y < 3, y \neq 1$ is a parameter that controls the behavior of the absorption and dispersion. For the forward (simulation) model, the inputs to this system of equations are the 2D fields corresponding to c_0 , the acoustic velocities; ρ_0 , the ambient densities; and α_0 , the attenuation. The output is the pressure p measured at the locations r_j of the transducers as a function of time, t . These measurements are then concatenated to form the measurement vector y . Abstractly, we can represent this forward model relationship as

$$y = f(c_0, \rho_0, \alpha_0) .$$

Using these equations we can solve for the pressure at the transducer locations for a given input signal in order to simulate the received signal. However, the inversion of the underlying quantities from the received signals based on this model is challenging because of the complicated and non-linear nature of the forward model.

To address these challenges, we developed a simplified linear model for the measurements [39], given by

$$\tilde{y}_{i,j}(t) = \int_{\mathbb{R}^3} \tilde{A}_{i,j}(\tau_{i,j}(\nu), t) \tilde{x}(\nu) d\nu + \tilde{d}_{i,j}(t),\tag{2.2}$$

where $\tilde{y}_{i,j}$ is the measurement at the transmit-receive pair (i, j) , ν is a point in the field of view, $\tilde{A}_{i,j}$ is a response function that accounts for the time-shift and attenuation of the transmitted pulse, \tilde{x} is the reflection coefficient, $\tau_{i,j}$ is the time delay of the

transmitted signal for point ν and the measurement pair (i, j) , $\tilde{d}_{i,j}$ is the direct arrival signal. Using this model, we designed a fast model-based reconstruction approach [39] (MBIR) which works by minimizing the cost-function

$$\hat{v} \leftarrow \underset{v}{\operatorname{argmin}} \left\{ \frac{1}{2} \|y - Av\|_2^2 + R(v) \right\}, \quad (2.3)$$

where A is a projection matrix which discretizes \tilde{A} , v is a vector of reflection coefficients and R is a Markov random field based regularizer [59]. While this model is simple and significantly improves the reconstructions compared to conventional delay-and-sum approaches like SAFT, the method can result in artifacts in the reconstructed images due to the assumption of linearity. Furthermore, the reflection coefficient may not have a clear quantitative interpretation compared to quantities such as the speed, density or attenuation in the medium.

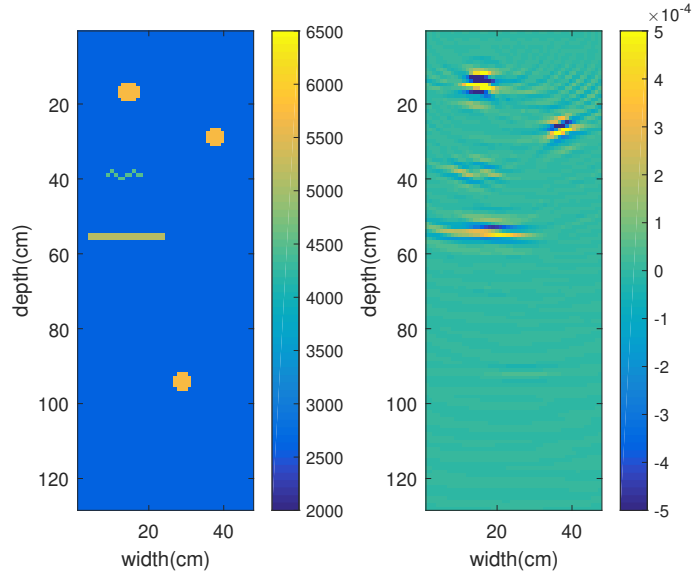


Fig. 2.3. Illustration of a back-projection of a one-sided ultrasonic NDE measurements using the system matrix A in Eq. 2.3. The left image is the ground truth (speed-of-sound in units of m/s) and the right image is the back-projection of the simulated measurements obtained from the ground truth using an array of 10 transducers and a non-linear wave propagation model. The back-projection suffers from artifacts and does not faithfully reconstruct the object.

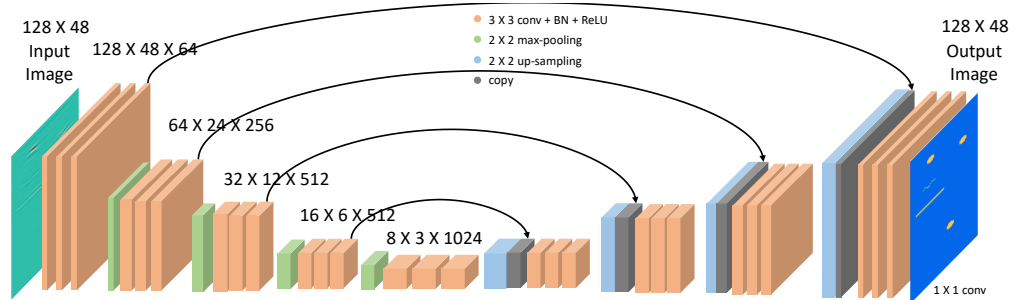


Fig. 2.4. DDL architecture used for the reconstructions. The input is an image obtained by applying the adjoint of a linear operator to the measurements. Within each stage, we apply a 3×3 convolution followed by a batch normalization and a rectified linear unit. The size of the feature maps at each stage is noted in the image.

2.3 Direct Deep Learning for Non-Linear Ultrasound Inversion

Since computing the exact solutions to (2.1) is expensive, we propose a two stage approach to the inversion. In the first step we leverage our previously introduced linear model and use the A matrix in (2.3) to get the back-projection, i.e. $\tilde{v} = A^T y$. While this method highlights some of the essential features, such a reconstruction is not quantitative and has severe artifacts due to the non-linearity of the interaction between the ultrasound signal and specimen (see Fig. 2.3). In order to compensate for these artifacts, we use such an image as input to a deep-neural network that has been trained to map such an input to the actual image of the desired material properties such as the speed of sound in the medium. In particular, we use a modified U-net architecture in [60] to learn a mapping of this initial image to the actual reconstruction (see Fig. 2.4). This architecture is desirable because it has the entire input image in its receptive field and can hence learn features that are globally correlated. Furthermore the presence of skip-connections ensures that the architecture combines the features from different scales effectively. We will refer to the proposed technique as direct deep learning (DDL) for the rest of the thesis.

Training of DDL using simulated data

We use the k-wave simulator to train DDL on one-sided UNDE applications [58]. The inputs to k-wave are three images: speed, density, and attenuation. The output of k-wave are measurement vectors where each vector corresponds to measurements from one transmit-receive pair. Fig. 2.5 shows an illustration of k-wave simulation where the output vectors are stacked to form one long vector. In this thesis, we vary the speed input and fix both the density and attenuation inputs for simplicity. We refer to this kind of noiseless dataset as pure-simulation-input (PSI) data. DDL is trained by inputting the back-projection of the k-wave measurements to the neural network and calculating the cost function of the output of the neural network and the ground truth speed image as shown in Fig. 2.6.

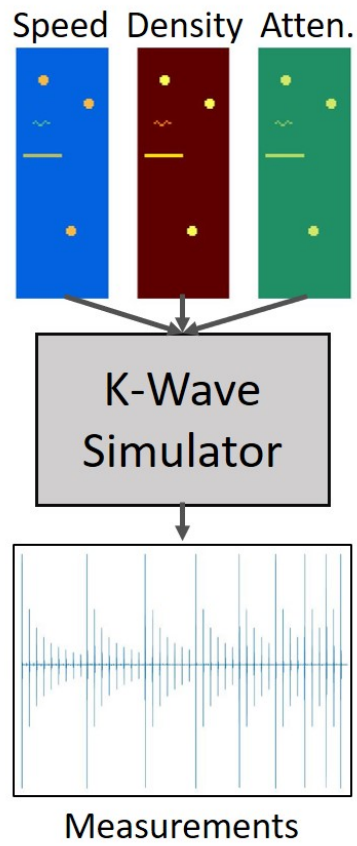


Fig. 2.5. Illustration of k-wave simulated data.

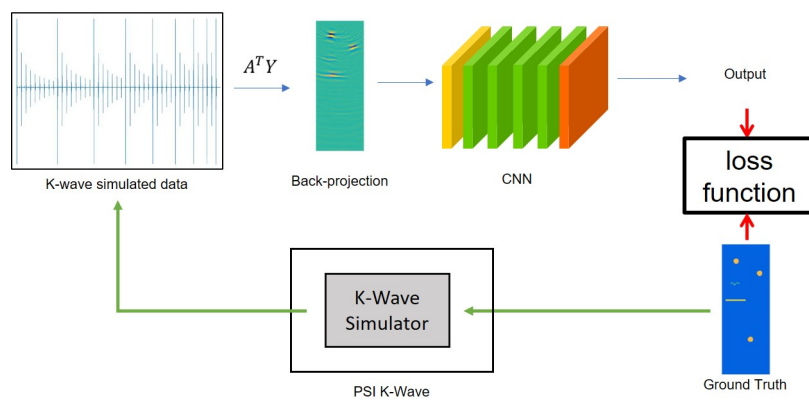


Fig. 2.6. Illustration of DDL training from k-wave PSI training data.

2.4 Modeling Mismatch

DDL is trained on simulated data because we don't have enough real data for training. However, this creates a problem which is a modeling mismatch between the k-wave simulation and the real data obtained in [39], see Fig. 2.7. Some of the reasons why the modeling mismatch is happening are as follows. First, the model for the transmitted signal used in k-wave is not sufficient enough to match the real transmitted signal in the experimental data. Currently, the best way to model the transmitted signal is to use either a clean direct arrival signal or a clean reflection from the experimental data. Next, k-wave does not model a transducer-surface coupling or any reverberations between defects and the concrete surface because it assumes the transducers are embedded in the medium. Next, another important reason is that we assume the concrete is a homogeneous medium in the k-wave simulation which is not the case in reality. This modeling mismatch does not effect the performance of SAFT or MBIR, but it is very critical in DDL because DDL will be trained on simulated data that do not sufficiently represent real data.

In this thesis, we propose a solution that reduces the effect of the modeling mismatch in the DDL training. We propose adding additive white Gaussian noise (AWGN) to the input of the simulation in the training set. We call this dataset noisy-simulation-input (NSI) data. Fig. 2.8 shows an illustration of the NSI k-wave block that needs to replace the PSI k-wave block in Fig. 2.6 to generate NSI data. Note that this solution does not reduce the modeling mismatch itself, but it reduces its effect. Furthermore, it makes DDL learn the general features of the system rather than very sophisticated features of k-wave simulation, i.e. the noise applied to the simulation input acts as a type of regularization to DDL. Also, note that the loss function for the DDL training uses the original ground truth not the noisy simulation input.

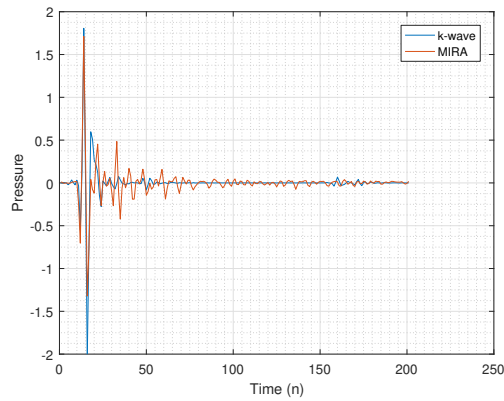


Fig. 2.7. Illustration of k-wave modeling mismatch with real data. The k-wave plot is from a k-wave simulation from a generated ground truth similar to a ground truth in the MIRA real data in [39].

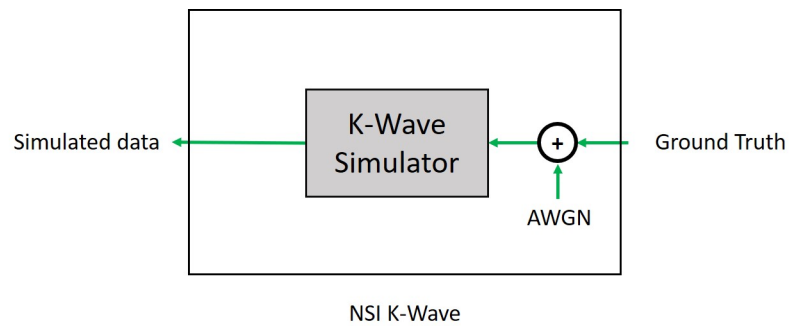


Fig. 2.8. Illustration of noisy-simulation-input (NSI) k-wave where AWGN is added to the input of k-wave before simulation. This block should replace the PSI k-wave block in Fig. 2.6 to generate NSI data.

2.5 Spatially Variant Amplification for Input In DDL

As the ultrasonic signal propagates through the medium, it gets attenuated considerably. This attenuation causes the reflection of deeper defects to be very weak. The convolutional layer in neural network is space invariant. Therefore, it is difficult to design an architecture based on convolutional layers that could account for the attenuation of deeper reflections. An issue in DDL appears when it mis-classifies weak reflections with steel rebars. The reason is that steel rebars are considered point scatterers, so their reflections are also weak, and DDL was trained on that. Furthermore, due to the weak reflections of deeper objects, many of these objects are classified as steel rebars in that region by DDL. To resolve this issue, we propose a spatially variant amplification (SVA) step where deeper regions of the back-projections are amplified more than closer regions. We adopt a similar formula used in MBIR for the spatially variant regularization [39], i.e.

$$c_s = 1 + (c_{max} - 1) \left(\frac{\text{Depth of } s}{\text{Maximum Depth}} \right)^a, \quad (2.4)$$

$$\tilde{v}_s \leftarrow \tilde{v}_s c_s, \quad (2.5)$$

where c_s is the amplification coefficient for pixel s , c_{max} is the the maximum amplification for the deepest region, a is a parameter that controls the transitioning from low amplification to high amplification, and \tilde{v}_s is the value of pixel s in the back-projection \tilde{v} .

2.6 Joint DDL

The DDL shown in section 2.3 is designed to reconstruct from a single scan. However, DDL is not designed for applications where multiple scans are obtained to reconstruct from a large field of view. For scanning large regions, typically, the ultrasonic device is used to perform multiples scans in raster order to build up a 3D profile of the structure, Fig. 2.9. A conventional stitching could be applied to stitch single DDL reconstructions, but this is not an efficient way to solve this

problem. In [39], MBIR used the joint-MAP technique to perform the stitching internally which turned out to be very efficient in reducing the stitching artifacts and exploiting extra information from adjacent scans. We are proposing a joint-DDL technique, an analogous approach to the joint-MAP technique in MBIR, that combines the back-projections of all the scans needed to reconstruct from the large field of view. The joint-DDL technique uses multiple input channels equal to the number of scans performed. However, the DDL architecture requires that the input size is the same as the output size which is not the case if each input channel has the size of a small single back-projection, and the output channel has the size of the large field of view. Therefore, joint-DDL makes the input channels have the same size as the output channels, but each input channel is set to zero everywhere except for the region where the scan is assumed to happen. This region is set to equal the back-projection of the corresponding scan. In this case, the non-zero region in each input channel is a shifted version of the region in the next or previous scan. The joint-DDL technique will require its architecture to be slightly different from DDL architecture, see Fig. 2.10. The first modification is the size of the input and output channel which will change to the size of the large field of view. The second modification is the number of input channel which will change from one to the number of scans obtained to cover the whole cross-section.

Training for Joint DDL

To train DDL on reconstructing multiple scans jointly, we need to generate multiple images that share the same cross section. Each cross section will be considered one training sample. If we use N independent cross-sections for the dataset, we need to simulate $N \times M$ images, where M is the number of images per cross-section. This is considered computationally expensive and inefficient. Independent cross-sections means that cross-sections do not share the same defects or targets. We are proposing a way to reduce the number of simulations needed while keeping the number of

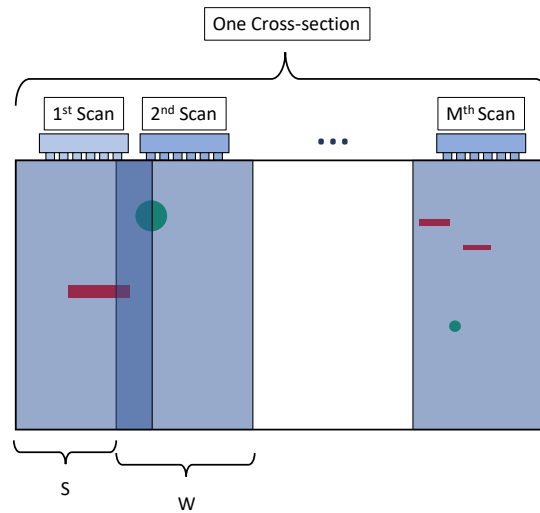


Fig. 2.9. An illustration of multiple measurements needed to scan a cross-section. Images from each scan share some pixels with its neighbor images. Proper stitching technique is needed to account for this shared areas in the field-of-view.

cross-sections, N , the same. The idea is to use dependent cross-sections. We use a significantly wide ground truth image with width equals to $W + (M + N - 2) \times S$, where W is the width of a single scan image, M is the number of images per cross-section, N is the number of cross-sections needed, and S is the length of the shift between each scan. Next, we assign each cross-section a unique M consecutive small images from the wide ground truth. Therefore, with this arrangement, we will only need to simulate $M + N - 1$ images to obtain N cross-sections for the DDL dataset, Figs. 2.9 and 2.11.

2.7 Results

In this section we compare DDL with two different techniques qualitatively and quantitatively.

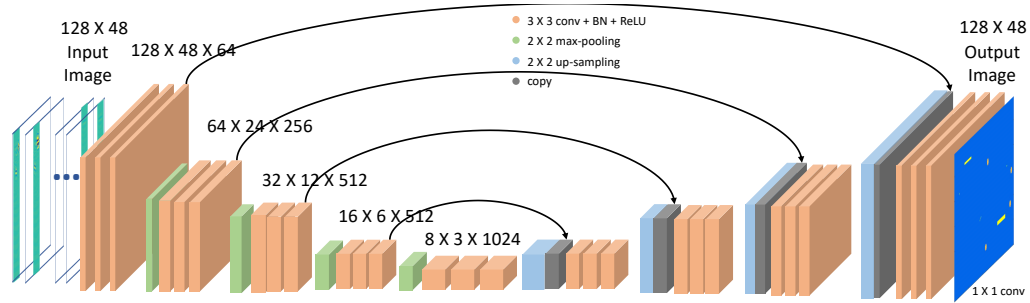


Fig. 2.10. Illustration of Joint-DDL architecture. Within each stage, we apply a 3×3 convolution followed by a batch normalization and a rectified linear unit. The size of the feature maps at each stage is noted in the image. The input to the neural network contains multiple channels where each channel is a back-projection of one of the scans shifted in the correct region where the scan was performed.

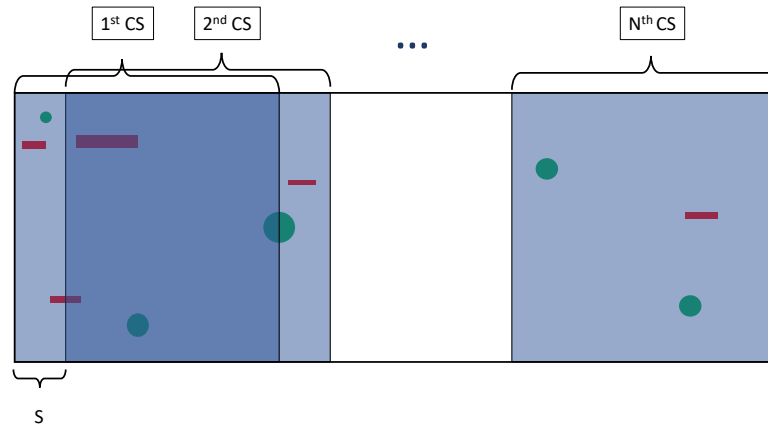


Fig. 2.11. An illustration of generating dataset of dependent cross-sections (CS). This helps in reducing the number of scans and simulations needed for DDL training.

2.7.1 Algorithms for Comparison

We compare DDL with SAFT [61] and MBIR [39] using simulated and experimental data. Both simulated and experimental data perform multiple scans to cover a large field of view. SAFT processes the multiple scans jointly while MBIR processes them using the joint-MAP stitching technique. For all MBIR qualitative results, the MBIR regularization parameters were tuned to show the best results visually.

DDL was trained on dataset that was generated by k-wave. k-wave simulates each single scan individually. The inputs to k-wave are 3 3D-ground-truth images of speed, density, and attenuation (we vary speed and fix density and attenuation) to simulate the propagation in 3D. The reason to use a 3D simulation is to model the attenuation of the propagated signal better and reduce the modeling mismatch as possible. The speed 3D-ground-truth image contains three layers that are duplicates of a 2D ground truth image. Next, the measurements were back-projected using the same system matrix used in MBIR. Note that the back-projection is in 2D not 3D. However, the size of the system matrix had to increase a little for DDL to account for the down-sampling in the architecture, i.e. the size changed from 120 x 210 cm to 128 x 224 cm. The reconstructed image is, then, cropped to return to the actual size of the field of view. Next, the back-projections of the simulated dataset are normalized by the mean and standard deviation of the back-projections of the training set. However, the back-projections of the experimental data are normalized by the mean and standard deviation of the back-projections of the experimental data. The mean and the variance are calculated without including the regions where the direct arrival artifacts might appear, e.g. the first 10 rows of all back-projections are ignored. Next, a spatially variant amplification is used to amplify deeper regions as described in section 2.5. The values we used for the parameters in Eq. 2.4 are $a = 3$ and $c_{max} = 10$. Finally, joint-DDL is used to reconstruct from the multiple scans in both simulated and experimental data.

The signal-to-noise-ratio (SNR) will be used for one DDL training and for comparison between the techniques. We define SNR to be

$$SNR = 10 \log_{10} \left(\frac{\|y\|^2}{\|w\|^2} \right),$$

where y is the noiseless simulated output from k-wave, and w is the added noise to y .

In this section, we will use two different DDL trainings: DDL trained on pure-simulation-input data (PSI-DDL) and DDL trained on noisy-simulation-input data where AWGN is added to the simulation input with $SNR = 0$ (NSI-DDL) as discussed in section 2.4. The training diagram for these different datasets is shown in Figs. 2.6 and 2.8.

The datasets were generated from dependent cross-sections. For each dataset, 1600, 200, and 200 cross-sections from the dataset were used for DDL training, validation, and testing, respectively. For DDL, we used the PyTorch [62] library, and the code for the neural network architecture was obtained from [63]. Stochastic gradient descent is used to optimize the loss function with batch size = 1, learning rate = 0.0001, and momentum = 0.5. Fig. 2.12 shows examples of the training phantoms used to generate the ultrasound training data along with the curves for training and validation plots for the data-set.

A component-wise precision and recall (PR) plot is used for the simulated and experimental data to compare the performance of each technique as shown in [39]. The number of true positive (TP), false positive (FP), and false negative (FN) for each technique are calculated using this metric. Using these values, the precision and recall curve can be plotted as follows:

$$recall = \frac{TP}{TP + FN}$$

and

$$precision = \frac{TP}{TP + FP}.$$

the techniques are compared by the area under the PR curves where larger area indicates better performance. The standard Matlab functions “edge(x,’log’,0)” and

“`imfill(x, 'holes')`”, where x is the image we would like to segment, are used to segment the reconstructed image into connected components. However, since DDL images has an offset of the background acoustic speed, e.g. 2620 m/s for concrete, DDL images are modified in the following way:

$$x \leftarrow |x - 2620|,$$

where x is the original DDL image. Next, for each connected component, the maximum value and centroid is calculated and stored. Next, each connected component is paired with a target if its centroid is the closest to the target’s centroid and if it is within a range r cm from the target. Note that targets or connected components cannot be paired more than once. There are two factors that can help in choosing the value of r . The first factor is the error margin of the true location of the targets (e_{gt}). There is no error margin in simulated data because the centroid of the targets are well known, so e_{gt} is zero, but in experimental data, e_{gt} is not zero. The second factor, is the average error margin of the target’s reconstructed centroid for all techniques (e_r). Typically, r is chosen to be the sum of the two error margins. Next, All images are divided by their maximum value for each technique. Next, thresholds from 1 to 0 with step 0.001 are applied to all images. For each threshold, a TP is declared if the maximum value of a paired connected component is equal or greater than the threshold. A FP is declared if the maximum value of an unpaired connected component is equal or greater than the threshold. The FN is calculated by subtracting the number of TP’s from the number of targets.

We used 2.60GHz Sky Lake CPUs and Tesla P100 GPUs. SAFT was performed using Matlab. MBIR was performed using C. DDL was performed using C (first step) and python (second step). The code for both MBIR and DDL was optimized for fast performance.

The simulation for both PSI and NSI datasets using k-wave required a total of about 48 hours using 96 CPUs and 12 GPUs. The DDL was trained two times for PSI and NSI where each training performed 100 epochs and required about 3.5 hours using one GPU.

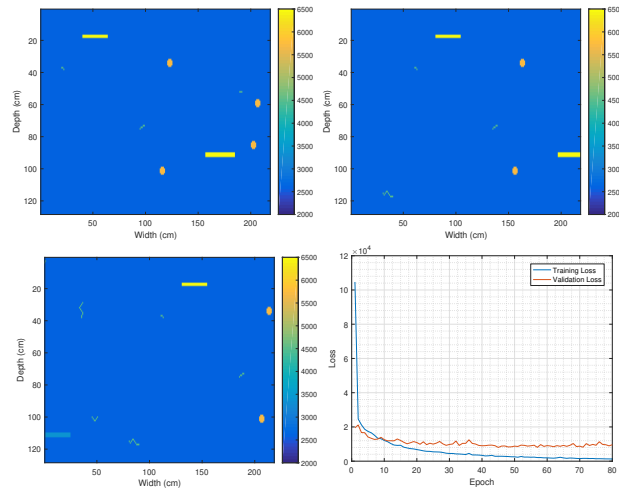


Fig. 2.12. Example of training phantoms used to train DDL and a plot of the training and validation loss vs. epoch.

For each cross-section reconstruction, SAFT required approximately 1 seconds using one CPU. MBIR required on average approximately 19 seconds using one CPU. The first step in DDL required approximately 0.54 seconds using one CPU. The second step in DDL required approximately 1.8 seconds using one CPU, or about 0.16 seconds using one GPU.

2.7.2 K-wave Simulated Results

In this section, we generate PSI data by simulating a system that is similar to the MIRA experiment performed in [39]. We used a ten transducer multi-static system with an acquisition geometry in which one of the transducers transmits while the others receive. The transducers are spaced 4 cm apart. The transmitter sends a pulse of duration 50 μ s with a carrier frequency of 52 KHz. The receiver collects 201 samples with a sampling frequency of 200 KHz.

The PSI dataset was generated by the k-Wave simulation software with its default boundary conditions [58] and is representative of the type of defects seen while inspecting thick, reinforced concrete walls with embedded steel plates. The density

and attenuation were fixed, while the speed of sound varied from pixel to pixel depending on the material of the object. The background of the field of view is concrete with acoustic speed of 2620 m/s. The steel rebar is represented as circles with speed 5660 m/s. The defects are represented as rectangles with different speeds with possible alkali-silica reactions (ASR) [64, 65] inside with speed 4500 m/s. The cracks are represented as ASR crooked lines. We used a wide ground truth (for dependent cross-sections) for the dataset as discussed in section 2.6, so we can take multiple scans where each scan is shifted by 10 cm from the previous or next scan. Each cross-section is assigned a unique 18 consecutive images of size 128×48 from the wide ground truth.

Fig. 2.13 shows reconstructed images from the test set (not used in training or validation) using SAFT, the linear MBIR of (2.3), PSI-DDL, and NSI-DDL techniques. PSI-DDL is trained from the training set of the PSI data. NSI-DDL is trained on the training set of the NSI data which is the same as the PSI data except that we add noise to the simulation input. Table 2.1 and Table 2.2 show the settings of all techniques. Fig. 2.14 and Table 2.3 show the component-wise PR results for each techniques over the results from the entire PSI testing set where PSI-DDL has the highest PR area. The error margin e_{gt} with these results is zero, but e_r is high because of SAFT's inaccuracy. Therefore, the range r for the PR metric was chosen to be 4 cm where lower values of r produce much poorer performance for SAFT with respect to the other techniques.

Fig. 2.15 shows the performance of all techniques in reconstructing sample 1 in Fig. 2.13 with AWGN added to the measurements of sample 1 with different SNR values.

Fig. 2.16 shows the performance of all techniques in reconstructing sample 1 in Fig. 2.13 with fewer measurements. The original number of measurement uses 45 distinct transmitter-receiver pairs for each scan.

Discussion

In Fig. 2.13, the units of each method are different, i.e. the unit in SAFT, MBIR, and DDL are pressure, reflectivity, and speed of sound, respectively. What makes DDL advantageous is that we are reconstructing the same unit as the ground truth which makes it easy to interpret the image. Notice that PSI-DDL reconstruction significantly outperforms SAFT and MBIR in reconstructing the targets with shape very close to the targets' true shape, and in reducing artifacts found in SAFT and MBIR. Sample 4 shows an important example where PSI-DDL was able to reduce the reverberation and shadowing artifacts significantly compared with SAFT and MBIR. NSI-DDL does not perform as good as PSI-DDL because we are intentionally adding noise to the simulation input in the training. This noisy simulation input degrades the performance of NSI-DDL, but it will enhance the performance when modeling mismatch is an issue, specially with real data.

In Fig. 2.15, MBIR reduces noise better than the other techniques. In general, targets in NSI-DDL appear more clearly. However, the noise in PSI-DDL and NSI-DDL are shown as circular or ASR objects similar to the ones it was trained on. Such noise may be hard to spot and may pass as actual features in the specimen.

In Fig. 2.16, PSI-DDL and NSI-DDL show better results overall than the other methods in showing the targets clearly with less noise and artifacts. However, similar to SAFT, PSI-DDL and NSI-DDL show artifacts at the top of the image caused by the direct arrival signal. The reason this is happening in PSI-DDL and NSI-DDL is because they were trained on removing the direct arrival artifacts from 45 pairs. With fewer pairs, the overlapping of the direct arrival artifacts is different to DDL which makes the artifact problem difficult to resolve.

2.7.3 MIRA Experimental Results

We are using the same MIRA experimental data demonstrated in [39] that was used mainly to compare MBIR with SAFT. In this thesis, we apply DDL to the

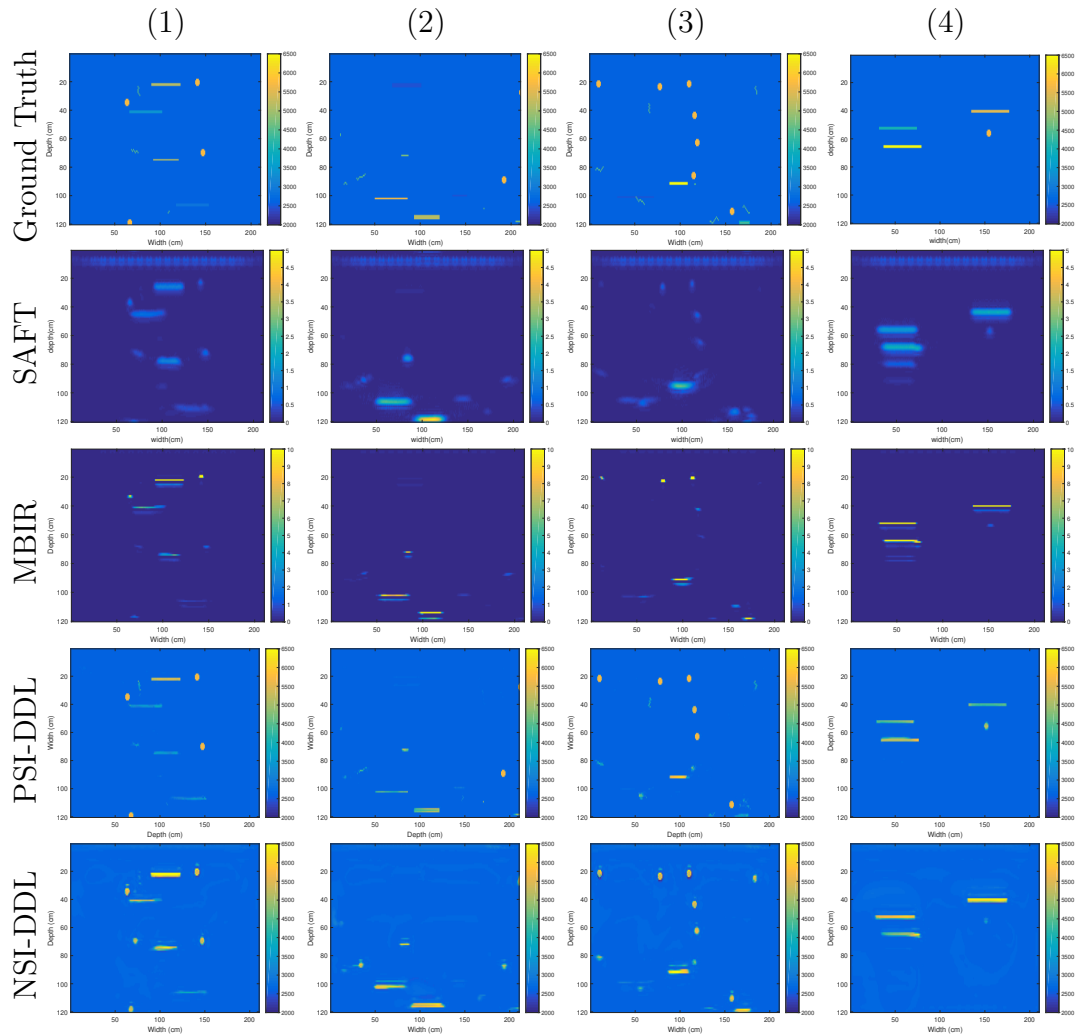


Fig. 2.13. Comparison between all reconstruction results from k-wave simulated data from the test set only: the first row is the ground truth, the second row is SAFT reconstruction, the third row is linear MBIR reconstruction, the fourth row is PSI-DDL reconstruction, and the fifth row is NSI-DDL reconstruction. PSI-DDL is outperforming the other techniques in showing target shapes much closer to the ground truth shapes.

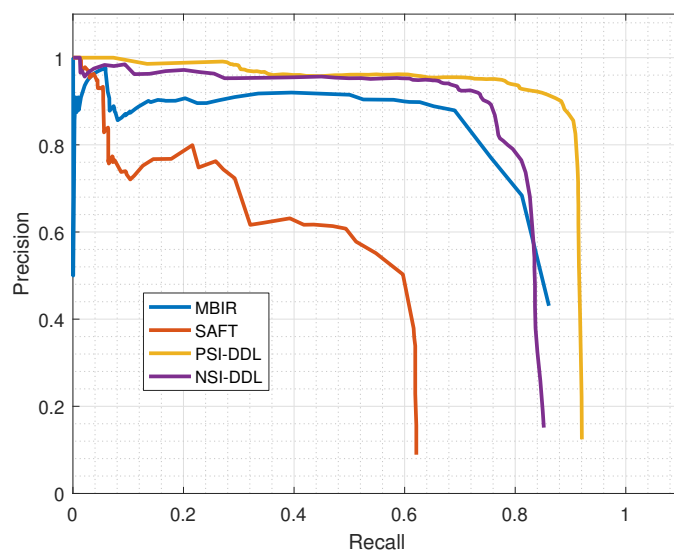


Fig. 2.14. PR plots for results from the entire k-wave PSI testing data.

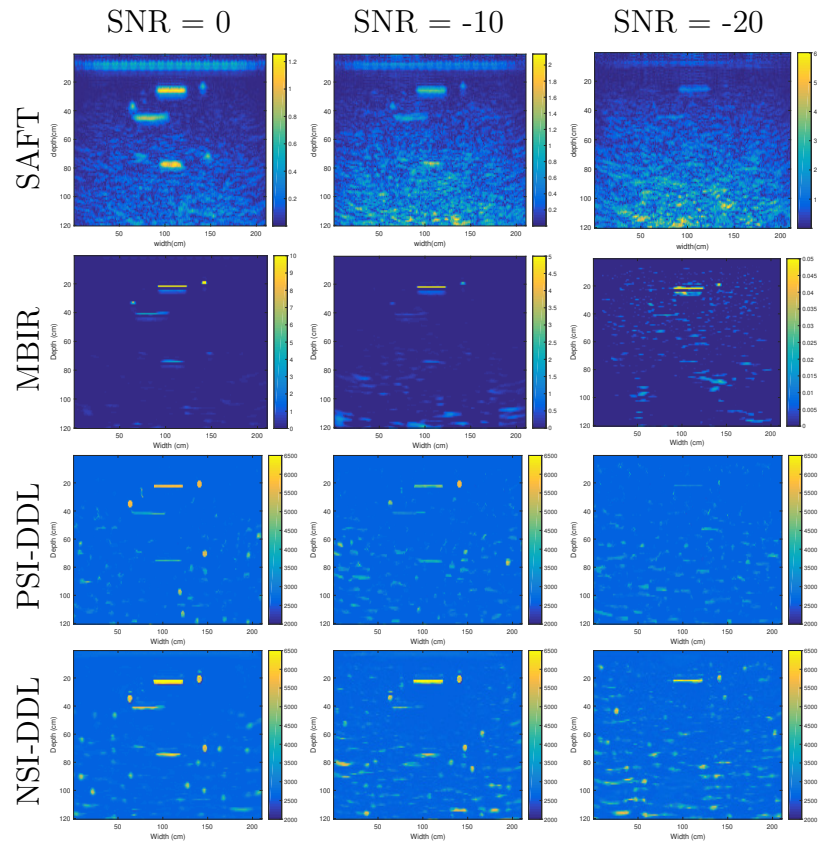


Fig. 2.15. Comparison between all techniques on reconstructing sample 1 in Fig. 2.13 with AWGN added to the measurements of sample 1 with different SNR values: the first row is SAFT reconstruction, the second row is linear MBIR reconstruction, the third row is PSI-DDL reconstruction, and the fourth row is NSI-DDL reconstruction.

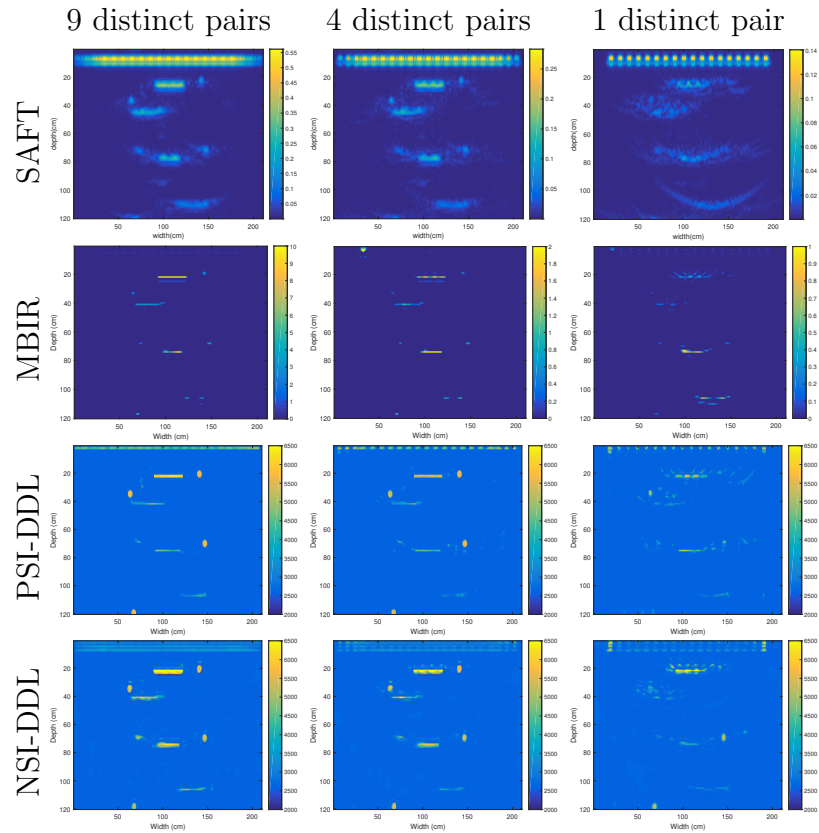


Fig. 2.16. Comparison between all techniques on reconstructing sample 1 in Fig. 2.13 with different number of transmitter-receiver pairs (less than 45 distinct pairs) per scan: the first row is SAFT reconstruction, the second row is linear MBIR reconstruction, the third row is PSI-DDL reconstruction, and the fourth row is NSI-DDL reconstruction.

MIRA data and compare its performance with the same SAFT and MBIR results previously published. The experiment extracted real data from a large concrete block of size 213.36 x 213.36 x 101.6 cm (84 x 84 x 40 inches), Fig. 2.17. The specimen was heavily reinforced with horizontal and vertical steel rebars and was embedded with designed defects in different locations, Fig. 2.18. However, the location of the targets are not exact due to possible displacement of the targets while pouring the cement. The specimen was scanned from both sides horizontally and vertically. Each cross-section required 18 scans with about 10-cm shift to cover the whole field of view. A total of 1314 scans were performed to cover 73 cross-sections of the specimen.

The MIRA device, Fig. 2.17, is used to collect the data [33, 34]. It contains 10 columns of transducers separated by 4 cm where each column contains 4 dry contact points with 2 mm radius. Only the distinct pairs, 45 pairs, are used in the reconstruction results for all techniques. The carrier frequency is 52 KHz, the speed of sound in concrete is 2620 m/s, and the sampling frequency is 200 KHz.

Four techniques were used to reconstruct the data: SAFT, MBIR, PSI-DDL, and NSI-DDL. For each cross-section, the techniques reconstruct the 18 scans jointly.

Fig. 2.19 shows the reconstruction for each technique. The first row shows the defect diagram. The second row shows the instantaneous envelop of SAFT reconstruction. The third row shows MBIR reconstruction. The fourth row shows PSI-DDL reconstruction. The fifth row shows NSI-DDL reconstruction.

Fig. 2.20 and Table 2.3 show the component-wise PR results for each technique over the whole 73 cross-sections where r is set to 10 cm because the position of the targets was not exactly known due to possible displacement while pouring the cement. NSI-DDL shows larger PR area than the other techniques. The MBIR PR area was optimized with respect to σ_g for a fair comparison.

Discussion

The results in Fig. 2.19 show significant enhancement for MBIR and NSI-DDL over SAFT in reducing noise and artifacts. Furthermore, NSI-DDL tends to show targets shape closer to the real shape than MBIR, e.g. circular steel rebars, rectangular defects, and a line for the back wall. In general, NSI-DDL tends to show targets more clearly and MBIR tends to have less noise.

NSI-DDL was able to reduce reverberation artifacts better than the other techniques. For example, NSI-DDL was able to resolve the reverberation caused by the edges of D-8, D-9, D-12, and D-13. However, NSI-DDL was not able to resolve the reverberation between the targets and the surface. This is because k-wave does not model transducer-surface coupling as discussed in section 2.4. Also, the shadowing artifacts appear mostly in the back wall for all techniques where a target can overshadow the back wall. The back wall in NSI-DDL tends to appear better behind targets than the other techniques.

The performance of NSI-DDL is better than PSI-DDL because NSI-DDL reduces the modeling mismatch issue which is a major problem in DDL.

2.7.4 Results from Spatially Variant Amplification

In this section we show results for sample 1 in Fig. 2.19 before and after the spatially variant amplification upgrade. Fig. 2.21 shows the results where (a) shows NSI-DDL without SVA and (b) shows NSI-DDL with SVA.

Discussion

The image in (a) shows reconstruction where deeper regions are attenuated and have circular artifacts because of the weak reflections from these regions. The image in (b) shows better reconstruction for deeper regions.

Table 2.1.

Parameter settings used for all techniques for the k-wave and the MIRA data.

Parameters	Value	Unit
Carrier frequency	52	<i>kHz</i>
Sampling frequency	200	<i>kHz</i>
Cement p-wave speed	2620	<i>m/s</i>
Reconstruction resolution	1	<i>cm</i>
Number of columns	210	-
Number of rows	120	-

Table 2.2.

The MBIR parameters settings used for the k-wave and the MIRA data.

Parameters	Value (K-wave/MIRA)	Unit
ϵ	0.01	-
α_0	30	$(MHz \cdot m)^{-1}$
p	1.1	-
q	2	-
T	1	-
c_{max}	10	-
a	3	-
σ_g	0.5/3	m^{-3}
σ_e	15	m^{-3}



Fig. 2.17. The concrete specimen and the MIRA device used for the experimental data [33]. 20 defects are embedded in the specimen.

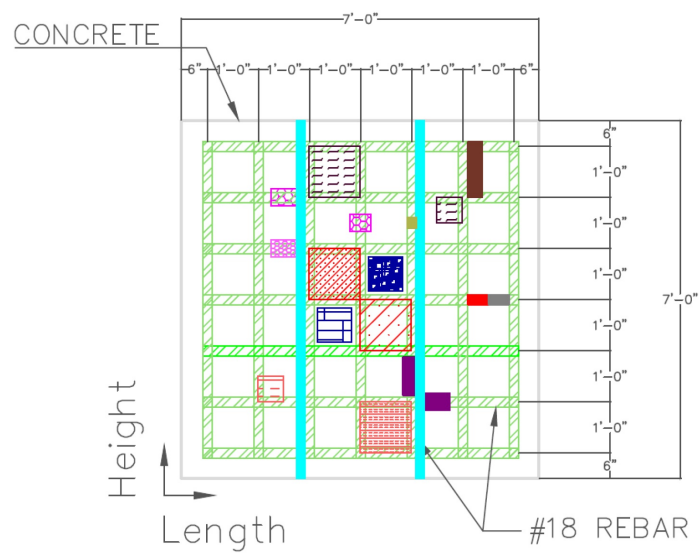


Fig. 2.18. A side view of defects [33]. The location of the defects is approximated due to possible displacement while pouring the cement.

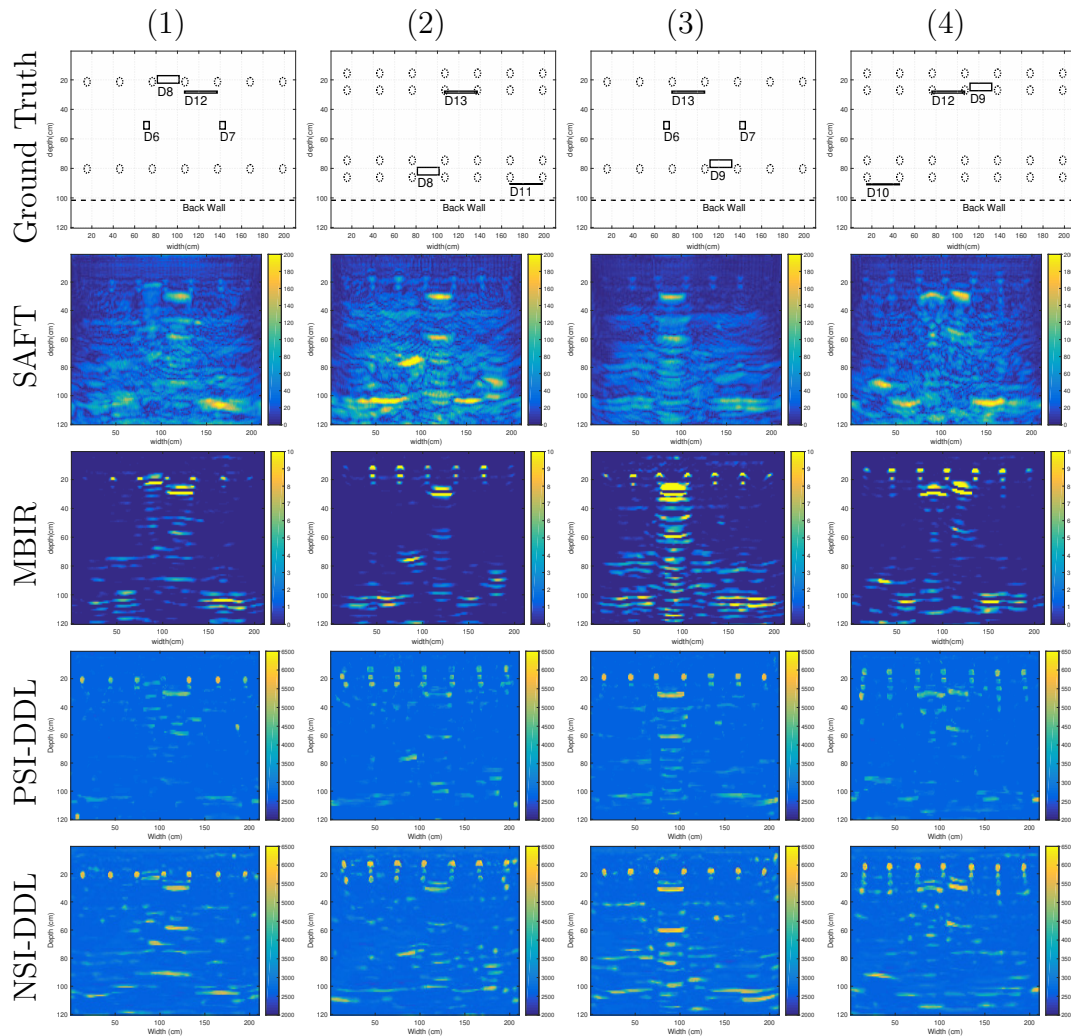


Fig. 2.19. Comparison between all techniques in reconstructing real data: the first row is the ground truth, the second row is SAFT reconstruction, the third row is linear MBIR reconstruction, the fourth row is PSI-DDL reconstruction, and the fifth row is NSI-DDL reconstruction. MBIR appears to have less noise while NSI-DDL appears to show more targets and less artifacts. The reconstructed targets in NSI-DDL have closer shapes to the real targets.

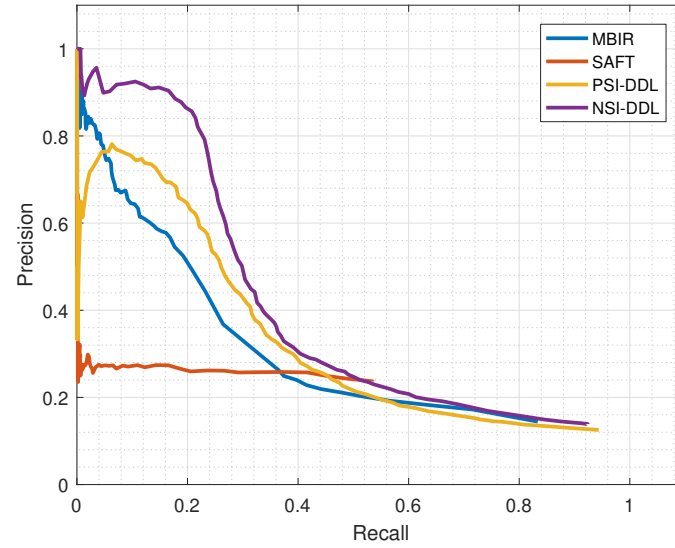


Fig. 2.20. PR plots for the entire MIRA experimental results.

Table 2.3.

Precision vs recall area for all techniques in Fig. 2.14 and Fig. 2.20. DDL has the highest PR area.

	SAFT	MBIR	PSI-DDL	NSI-DDL
PR area for k-wave data	0.4264	0.7471	0.8818	0.7883
PR area for MIRA data	0.1397	0.2836	0.3255	0.3936

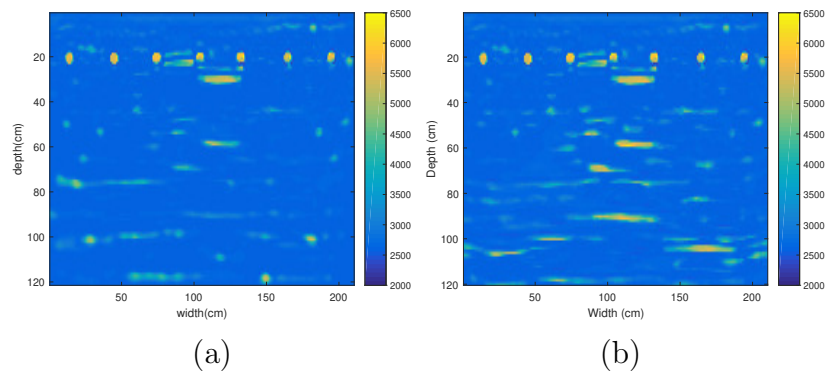


Fig. 2.21. Results for sample 1 in Fig. 2.19 for DDL with and without SVA. (a) is NSI-DDL without SVA and (b) is NSI-DDL with SVA.

2.8 Summary

In this thesis, we proposed a method for reflection model ultrasound reconstruction using a deep neural network. Our algorithm obtains an initial estimate using a linear back projection and then uses a trained neural network to map this preliminary reconstruction to the final solution. We proposed a solution to resolve the modeling mismatch in the K-wave simulation by adding noise to the simulation input. We also used a spatially variant amplification to amplify reflections for deeper regions which helps in reducing artifacts and detect more targets in those regions. We proposed joint DDL that jointly reconstructs multiple scans which share the same cross-section. Finally, using simulated and experimental data we showed that our algorithm produces a significant improvement quantitatively and qualitatively compared to the typically used analytic algorithms as well as iterative algorithms based on linear models.

REFERENCES

REFERENCES

- [1] P. Ramuhalli, J. W. Griffin, R. M. Meyer, S. G. Pitman, J. M. Fricke, M. E. Dahl, M. S. Prowant, T. A. Kafentzis, J. B. Coble, and T. J. Roosendaal, *Non-destructive Examination (NDE) Detection and Characterization of Degradation Precursors, Technical Progress Report for FY 2012*. Washington, D.C. : United States. Office of the Assistant Secretary for Nuclear Energy ; Oak Ridge, Tenn. : distributed by the Office of Scientific and Technical Information, U.S. Dept. of Energy, 2012.
- [2] M. Berndt, “Non-destructive testing methods for geothermal piping.” 2001.
- [3] J. Zemanek, E. E. Glenn, L. J. Norton, and R. L. Caldwell, “Formation evaluation by inspection with the borehole televiewer,” *Geophysics*, vol. 35, no. 2, pp. 254–269, 1970.
- [4] K. Hoegh and L. Khazanovich, “Extended synthetic aperture focusing technique for ultrasonic imaging of concrete,” *NDT and E International*, vol. 74, p. 33–42, 2015.
- [5] T. Stepinski, “An implementation of synthetic aperture focusing technique in frequency domain,” *ieee transactions on ultrasonics, ferroelectrics, and frequency control*, vol. 54, no. 7, 2007.
- [6] M. Li and G. Hayward, “Ultrasound Nondestructive Evaluation (NDE) imaging with transducer arrays and adaptive processing,” *Sensors*, vol. 12, no. 12, p. 42–54, 2011.
- [7] J. Haldorsen, D. Johnson, T. Plona, B. Sinha, H. Valero, and K. Winkler, “Borehole acoustic waves,” *Oilfield Review*, vol. 18, no. 1, pp. 34–43, 2006.
- [8] Z. Shao, L. Shi, Z. Shao, and J. Cai, “Design and application of a small size SAFT imaging system for concrete structure,” *Review of Scientific Instruments*, vol. 82, no. 7, p. 073708, 2011.
- [9] B. J. Engle, J. L. W. Schmerr, and A. Sedov, “Quantitative ultrasonic phased array imaging,” *AIP Conf. Proc.*, vol. 1581, no. 7, p. 49, 2014.
- [10] G. Dobie, S. G. Pierce, and G. Hayward, “The feasibility of synthetic aperture guided wave imaging to a mobile sensor platform,” *NDT and E International*, vol. 58, no. 7, pp. 10–17, 2013.
- [11] S. Beniwal and A. Ganguli, “Defect detection around rebars in concrete using focused ultrasound and reverse time migration,” *Ultrasonics*, vol. 62, p. 112–125, 2015.

- [12] M. Schickert, M. Krause, and W. Müller, “Ultrasonic imaging of concrete elements using reconstruction by synthetic aperture focusing technique,” *Journal of Materials in Civil Engineering*, vol. 15, no. 3, pp. 235–246, 2003.
- [13] E. Ozkan, V. Vishnevsky, and O. Goksel, “Inverse problem of ultrasound beamforming with sparsity constraints and regularization,” *IEEE transactions on ultrasonics, ferroelectrics, and frequency control*, vol. 65, no. 3, pp. 356–365, 2018.
- [14] H. Wu, J. Chen, S. Wu, H. Jin, and K. Yang, “A model-based regularized inverse method for ultrasonic B-scan image reconstruction,” *Measurement Science and Technology*, vol. 26, no. 10, p. 105401, 2015.
- [15] A. Tuysuzoglu, J. M. Kracht, R. O. Cleveland, M. Cetin, and W. C. Karl, “Sparsity driven ultrasound imaging a,” *The Journal of the Acoustical Society of America*, vol. 131, no. 2, pp. 1271–1281, 2012.
- [16] G. A. Guarneri, D. R. Pipa, F. N. Junior, L. V. R. de Arruda, and M. V. W. Zibetti, “A sparse reconstruction algorithm for ultrasonic images in nondestructive testing,” *Sensors*, vol. 15, no. 4, pp. 9324–9343, 2015.
- [17] T. Szasz, A. Basarab, and D. Kouamé, “Beamforming through regularized inverse problems in ultrasound medical imaging,” *IEEE transactions on ultrasonics, ferroelectrics, and frequency control*, vol. 63, no. 12, pp. 2031–2044, 2016.
- [18] H. M. Shieh, H.-C. Yu, Y.-C. Hsu, and R. Yu, “Resolution enhancement of nondestructive testing from b-scans,” *International Journal of Imaging Systems and Technology*, vol. 22, no. 3, pp. 185–193, 2012.
- [19] H. Almansouri, C. Johnson, D. Clayton, Y. Polsky, C. Bouman, and H. Santos-Villalobos, “Progress implementing a model-based iterative reconstruction algorithm for ultrasound imaging of thick concrete,” in *AIP Conference Proceedings*, vol. 1806, no. 1. AIP Publishing, 2017, p. 020016.
- [20] H. Almansouri, S. Venkatakrisnan, D. Clayton, Y. Polsky, C. Bouman, and H. Santos-Villalobos, “Anisotropic modeling and joint-map stitching for improved ultrasound model-based iterative reconstruction of large and thick specimens,” in *AIP Conference Proceedings*, vol. 1949, no. 1. AIP Publishing, 2018, p. 030002.
- [21] ———, “Ultrasonic model-based iterative reconstruction with spatially variant regularization for one-sided non-destructive evaluation,” *Electronic Imaging*, vol. 2018, no. 15, pp. 103–1, 2018.
- [22] A. Kak and K. A. Dines, “Signal processing of broadband pulsed ultrasound: Measurement of attenuation of soft biological tissues,” *IEEE Transactions on Biomedical Engineering*, vol. BME-25, no. 4, pp. 321–344, 1978.
- [23] S. J. Norton and M. Linzer, “Ultrasonic reflectivity imaging in three dimensions: Exact inverse scattering solutions for plane, cylindrical, and spherical apertures,” *IEEE Transactions on Biomedical Engineering*, vol. BME-28, no. 2, pp. 202–220, 1981.
- [24] J. W. Wiskin, “Inverse scattering from arbitrary two-dimensional objects in stratified environments via a Green’s operator,” *The Journal of the Acoustical Society of America*, vol. 102, no. 2, p. 853, 1997.

- [25] T. Huttunen, M. Malinen, J. Kaipio, P. White, and K. Hynynen, "A full-wave Helmholtz model for continuous-wave ultrasound transmission," *IEEE Transactions on Ultrasonics, Ferroelectrics and Frequency Control*, vol. 52, no. 3, p. 397–409, 2005.
- [26] T. Voigt, *The application of an ultrasonic shear wave reflection method for non-destructive testing of cement-based materials at early ages: an experimental and numerical analysis*. Books on Demand, 2005.
- [27] B. E. Treeby and B. T. Cox, "Fast tissue-realistic models of photoacoustic wave propagation for homogeneous attenuating media," *Photons Plus Ultrasound: Imaging and Sensing 2009*, Dec 2009.
- [28] B. E. Treeby, M. Tumen, and B. T. Cox, "Time Domain Simulation of Harmonic Ultrasound Images and Beam Patterns in 3D Using the k-space Pseudospectral Method," *Lecture Notes in Computer Science Medical Image Computing and Computer-Assisted Intervention – MICCAI 2011*, p. 363–370, 2011.
- [29] M. Li and G. Hayward, "Ultrasound nondestructive evaluation (nde) imaging with transducer arrays and adaptive processing," *Sensors*, vol. 12, no. 1, pp. 42–54, 2011.
- [30] C. Bouman, *Model Based Image Processing*, 1st ed. Purdue University, 2013.
- [31] Z. Yu, J.-B. Thibault, C. A. Bouman, K. D. Sauer, and J. Hsieh, "Fast model-based x-ray ct reconstruction using spatially nonhomogeneous icd optimization," *IEEE Transactions on image processing*, vol. 20, no. 1, pp. 161–175, 2011.
- [32] B. E. Treeby and B. T. Cox, "k-Wave: MATLAB toolbox for the simulation and reconstruction of photoacoustic wave fields," *Journal of biomedical optics*, vol. 15, no. 2, pp. 021 314–021 314, 2010.
- [33] D. A. Clayton, A. M. Barker, H. J. Santos-Villalobos, A. P. Albright, K. Hoegh, and L. Khazanovich, "Nondestructive evaluation of thick concrete using advanced signal processing techniques," Jan 2015.
- [34] K. Hoegh and L. Khazanovich, "Correlation analysis of 2d tomographic images for flaw detection in pavements," *Journal of Testing and Evaluation*, vol. 40, no. 2, pp. 247–255, 2011.
- [35] —, "Extended synthetic aperture focusing technique for ultrasonic imaging of concrete," *NDT & E International*, vol. 74, pp. 33–42, 2015.
- [36] D. Garcia, L. Le Tarnec, S. Muth, E. Montagnon, J. Porée, and G. Cloutier, "Stolt's fk migration for plane wave ultrasound imaging," *IEEE transactions on ultrasonics, ferroelectrics, and frequency control*, vol. 60, no. 9, pp. 1853–1867, 2013.
- [37] L. Le Jeune, S. Robert, E. L. Villaverde, and C. Prada, "Plane wave imaging for ultrasonic non-destructive testing: Generalization to multimodal imaging," *Ultrasonics*, vol. 64, pp. 128–138, 2016.
- [38] S. Bernard, V. Monteiller, D. Komatitsch, and P. Lasaygues, "Ultrasonic computed tomography based on full-waveform inversion for bone quantitative imaging," *Physics in Medicine & Biology*, vol. 62, no. 17, p. 7011, 2017.

- [39] H. A. Almansouri, S. Venkatakrisnan, C. A. Bouman, and H. Santos-Villalobos, “Model-based iterative reconstruction for one-sided ultrasonic non-destructive evaluation,” *IEEE Transactions on Computational Imaging*, pp. 1–1, 2018.
- [40] M. T. McCann, K. H. Jin, and M. Unser, “Convolutional neural networks for inverse problems in imaging: A review,” *IEEE Signal Processing Magazine*, vol. 34, no. 6, pp. 85–95, 2017.
- [41] Y. Han and J. C. Ye, “Deep residual learning approach for sparse-view CT reconstruction,” in *Fully Three-Dimensional Image Reconstruction in Radiology and Nuclear Medicine*. Fully3D conference organization, 2017.
- [42] K. H. Jin, M. T. McCann, E. Froustey, and M. Unser, “Deep convolutional neural network for inverse problems in imaging,” *IEEE Transactions on Image Processing*, vol. 26, no. 9, pp. 4509–4522, 2017.
- [43] Y. Han, J. Yoo, H. H. Kim, H. J. Shin, K. Sung, and J. C. Ye, “Deep learning with domain adaptation for accelerated projection-reconstruction MR,” *Magnetic resonance in medicine*, vol. 80, no. 3, pp. 1189–1205, 2018.
- [44] S. Wang, Z. Su, L. Ying, X. Peng, S. Zhu, F. Liang, D. Feng, and D. Liang, “Accelerating magnetic resonance imaging via deep learning,” in *Biomedical Imaging (ISBI), 2016 IEEE 13th International Symposium on*. IEEE, 2016, pp. 514–517.
- [45] S. Antholzer, M. Haltmeier, and J. Schwab, “Deep learning for photoacoustic tomography from sparse data,” *arXiv preprint arXiv:1704.04587*, 2017.
- [46] A. Hauptmann, F. Lucka, M. Betcke, N. Huynh, J. Adler, B. Cox, P. Beard, S. Ourselin, and S. Arridge, “Model based learning for accelerated, limited-view 3D photoacoustic tomography,” *IEEE transactions on medical imaging*, 2018.
- [47] A. Mousavi and R. G. Baraniuk, “Learning to invert: Signal recovery via deep convolutional networks,” in *Acoustics, Speech and Signal Processing (ICASSP), 2017 IEEE International Conference on*. IEEE, 2017, pp. 2272–2276.
- [48] Y. Sun, Z. Xia, and U. S. Kamilov, “Efficient and accurate inversion of multiple scattering with deep learning,” *Optics express*, vol. 26, no. 11, pp. 14 678–14 688, 2018.
- [49] S. V. Venkatakrisnan, C. A. Bouman, and B. Wohlberg, “Plug-and-play priors for model based reconstruction,” in *Global Conference on Signal and Information Processing (GlobalSIP), 2013 IEEE*. IEEE, 2013, pp. 945–948.
- [50] S. Sreehari, S. V. Venkatakrisnan, B. Wohlberg, G. T. Buzzard, L. F. Drummy, J. P. Simmons, and C. A. Bouman, “Plug-and-play priors for bright field electron tomography and sparse interpolation,” *IEEE Transactions on Computational Imaging*, vol. 2, no. 4, pp. 408–423, 2016.
- [51] K. Zhang, W. Zuo, S. Gu, and L. Zhang, “Learning deep cnn denoiser prior for image restoration,” in *2017 IEEE Conference on Computer Vision and Pattern Recognition (CVPR)*, July 2017, pp. 2808–2817.
- [52] H. Gupta, K. H. Jin, H. Q. Nguyen, M. T. McCann, and M. Unser, “CNN-based projected gradient descent for consistent CT image reconstruction,” *IEEE transactions on medical imaging*, vol. 37, no. 6, pp. 1440–1453, 2018.

- [53] J. Rick Chang, C.-L. Li, B. Póczos, B. Vijaya Kumar, and A. C. Sankaranarayanan, “One network to solve them all—solving linear inverse problems using deep projection models,” in *Proceedings of the IEEE Conference on Computer Vision and Pattern Recognition*, 2017, pp. 5888–5897.
- [54] J. Adler and O. Öktem, “Learned primal-dual reconstruction,” *IEEE transactions on medical imaging*, vol. 37, no. 6, pp. 1322–1332, 2018.
- [55] T. Meinhardt, M. Möller, C. Hazirbas, and D. Cremers, “Learning proximal operators: Using denoising networks for regularizing inverse imaging problems,” in *ICCV*, October 2017. [Online]. Available: <https://github.com/tum-vision/learn-prox-ops>
- [56] M. Feigin, D. Freedman, and B. W. Anthony, “A deep learning framework for single sided sound speed inversion in medical ultrasound,” *arXiv preprint arXiv:1810.00322*, 2018.
- [57] A. A. Nair, T. D. Tran, A. Reiter, and M. A. L. Bell, “A deep learning based alternative to beamforming ultrasound images,” in *2018 IEEE International Conference on Acoustics, Speech and Signal Processing (ICASSP)*. IEEE, 2018, pp. 3359–3363.
- [58] B. E. Treeby and B. T. Cox, “k-Wave: MATLAB toolbox for the simulation and reconstruction of photoacoustic wave-fields,” *J. Biomed. Opt.*, vol. 14, no. 2, pp. 021 314–12, 2010.
- [59] J.-B. Thibault, K. D. Sauer, C. A. Bouman, and J. Hsieh, “A three-dimensional statistical approach to improved image quality for multislice helical ct,” *Medical physics*, vol. 34, no. 11, pp. 4526–4544, 2007.
- [60] O. Ronneberger, P. Fischer, and T. Brox, “U-net: Convolutional networks for biomedical image segmentation,” in *International Conference on Medical image computing and computer-assisted intervention*. Springer, 2015, pp. 234–241.
- [61] Z. Shao, L. Shi, Z. Shao, and J. Cai, “Design and application of a small size soft imaging system for concrete structure,” *Review of Scientific Instruments*, vol. 82, no. 7, p. 073708, 2011.
- [62] A. Paszke, S. Gross, S. Chintala, G. Chanan, E. Yang, Z. DeVito, Z. Lin, A. Desmaison, L. Antiga, and A. Lerer, “Automatic differentiation in pytorch,” 2017.
- [63] T. Ho, “unet-pytorch,” <https://github.com/timctho/unet-pytorch/blob/master/Unet.py>, 2017.
- [64] P. Barnes and J. Bensted, *Structure and performance of cements*. CRC Press, 2014.
- [65] D. W. Hobbs, *Alkali-silica reaction in concrete*. London, 1988.

VITA

VITA

Hani Almansouri received his B.S. and M.S. in electrical and computer engineering from Purdue University, West Lafayette, IN, in 2010 and 2013, respectively. He is currently pursuing the Ph.D. degree in electrical and computer engineering at Purdue University, West Lafayette, IN. His research interests are in inverse problems, computational imaging, optimization, and deep learning.